Environmental Applications of Zeolites: Preparation and Screening of Cu-Modified Zeolites as Potential CO Sensors

Martin Jendrlin [1,*], Julien Grand [2], Louwanda Lakiss [2], Philippe Bazin [2], Svetlana Mintova [2] and Vladimir Zholobenko [1]

[1] School of Chemical and Physical Sciences, Keele University, Keele ST5 5BG, UK; v.l.zholobenko@keele.ac.uk
[2] Laboratoire Catalyse et Spectrochimie, ENSICAEN, CNRS, Normandie Université, 6 Bd Maréchal Juin, 14000 Caen, France; jgrand1985@gmail.com (J.G.); louwanda.lakiss@ensicaen.fr (L.L.); philippe.bazin@ensicaen.fr (P.B.); svetlana.mintova@ensicaen.fr (S.M.)
* Correspondence: m.jendrlin@keele.ac.uk

Supplementary information: CU CO SI

Table S1 Zeolite properties of the zeolites used in this work, Si/Al values were determined by the manufacturers, MR – membered ring

	Structure type	Si/Al	Pore Size, Å	Largest Channel, MR	Channel Network	Crystallite size, µm	Extraframework Cation
MOR	MOR (Mordenite)	10.0	6.7	12	1D	0.74	NH_4^+
BEA-12	BEA (Zeolite Beta)	12.5	6.8	12	3D	0.04	NH_4^+
BEA-19	BEA (Zeolite Beta)	19.0	6.8	12	3D	0.04	NH_4^+
ZSM-5	MFI (Mobil Type Five)	40.0	5.5	10	2D	0.52	NH_4^+
NaX	FAU (Faujasite)	1.3	7.4	12	3D	0.78	Na^+
NaY	FAU (Faujasite)	2.6	7.4	12	3D	0.78	Na^+
FER	FER (Ferrierite)	10.0	5.0	10	2D	0.6	Na^+

Figure S1 FTIR spectrometer and vacuum cell.

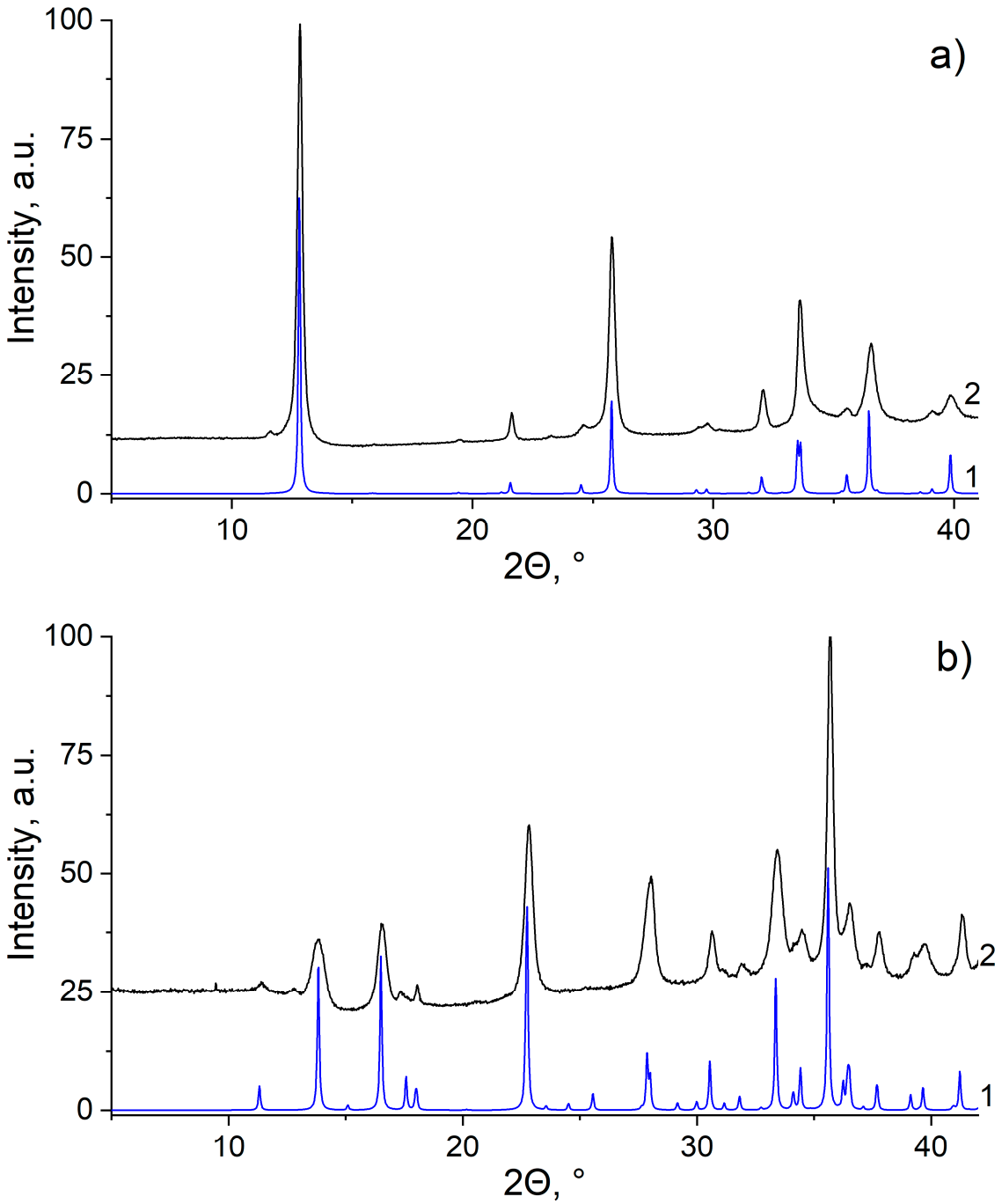
a)
Intensity, a.u.
100
75
50
25
0
10
20
30
40
2Θ, °
2
1
b)
Intensity, a.u.
100
75
50
25
0
10
20
30
40
2Θ, °
2
1

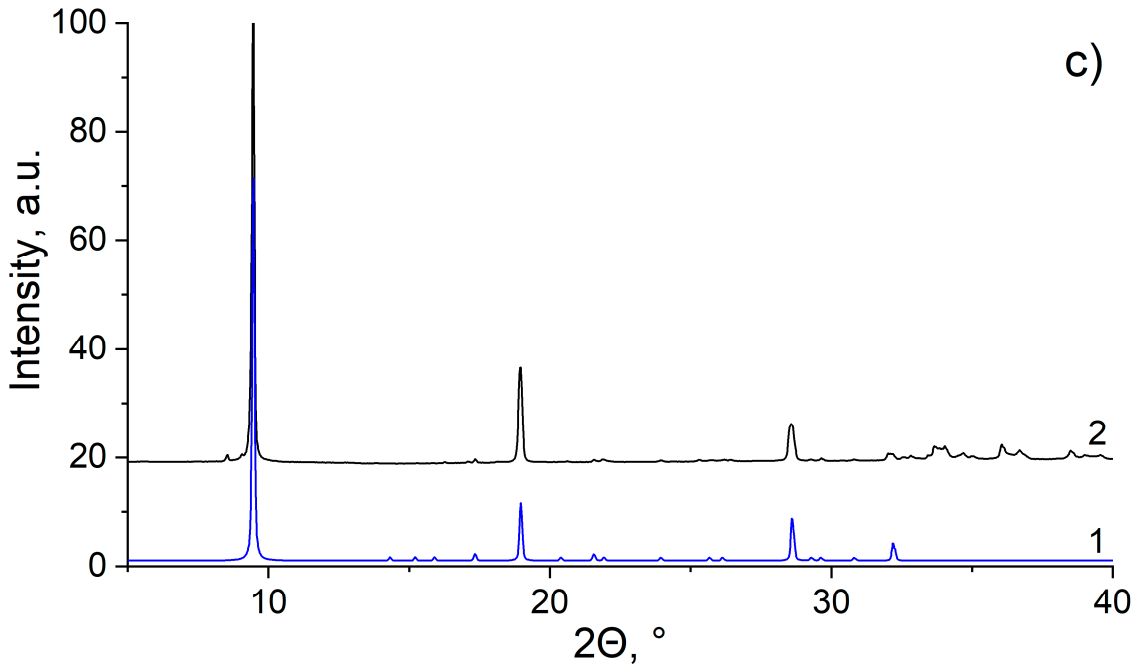

Figure S2 Calculated (1) and experimental (2) XRD patterns of $Cu_2(NO_3)(OH)_3$ (a), $CuSO_4 \cdot 3Cu(OH)_2$ (b) and $[Cu(OAc)_2]_2 \cdot Cu(OH)_2 \cdot 5H_2O$ (c); calculated patterns are simulated from the structures deposited in ICSD and ICDD

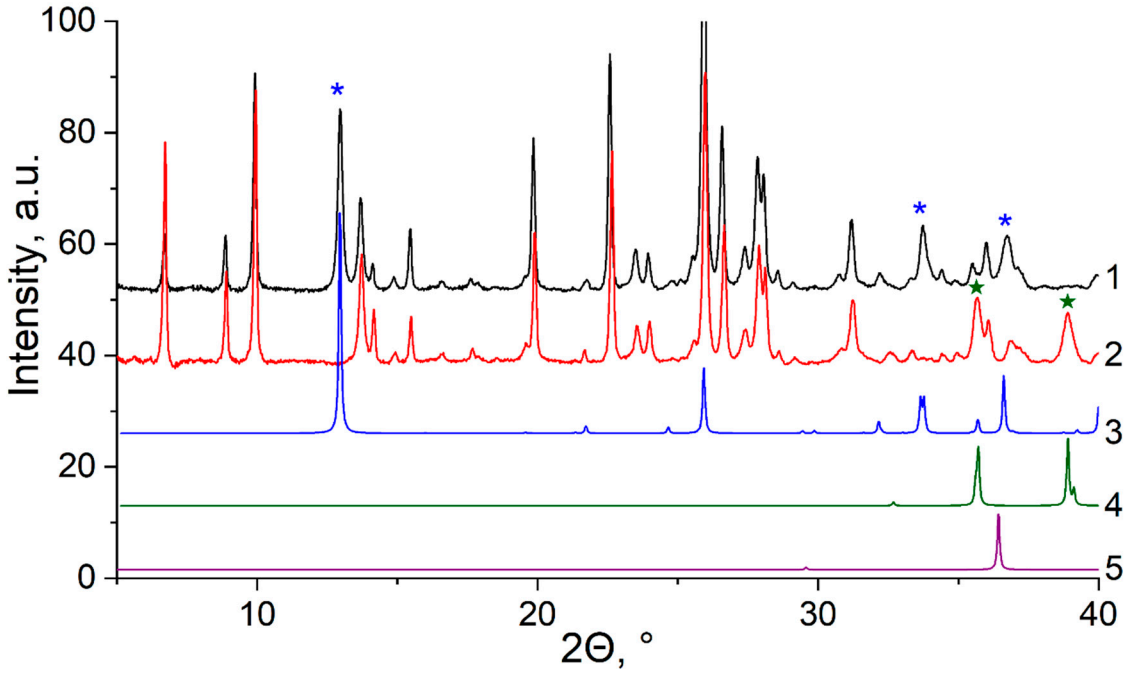

Figure S3 XRD patterns of MOR $Cu(NO_3)_2$ before activation (1), MOR $Cu(NO_3)_2$ after activation (2), the calculated pattern of $Cu_2(NO_3)(OH)_3$ (3), the calculated pattern of CuO (4), the calculated pattern of Cu_2O (5) patterns are offset and calculated patterns are scaled for clarity.

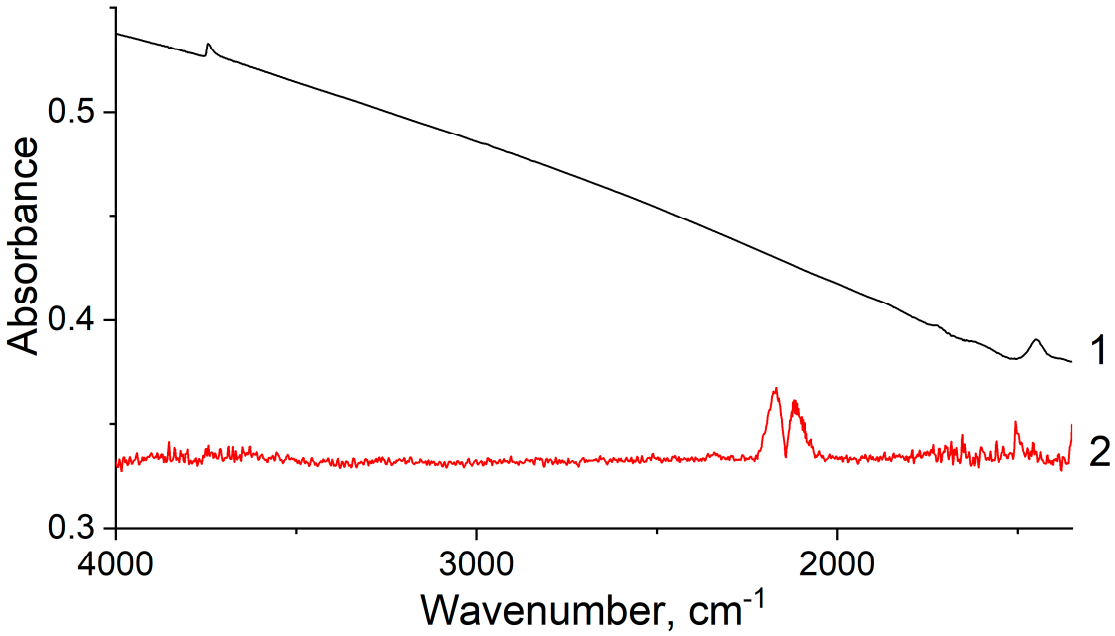

Figure S4 FTIR spectra of CO adsorbed on $Cu(NO_3)_2$-impregnated fumed silica (1) and 5000 ppm of CO* (2), * spectrum is offset and multiplied by 5 for clarity.

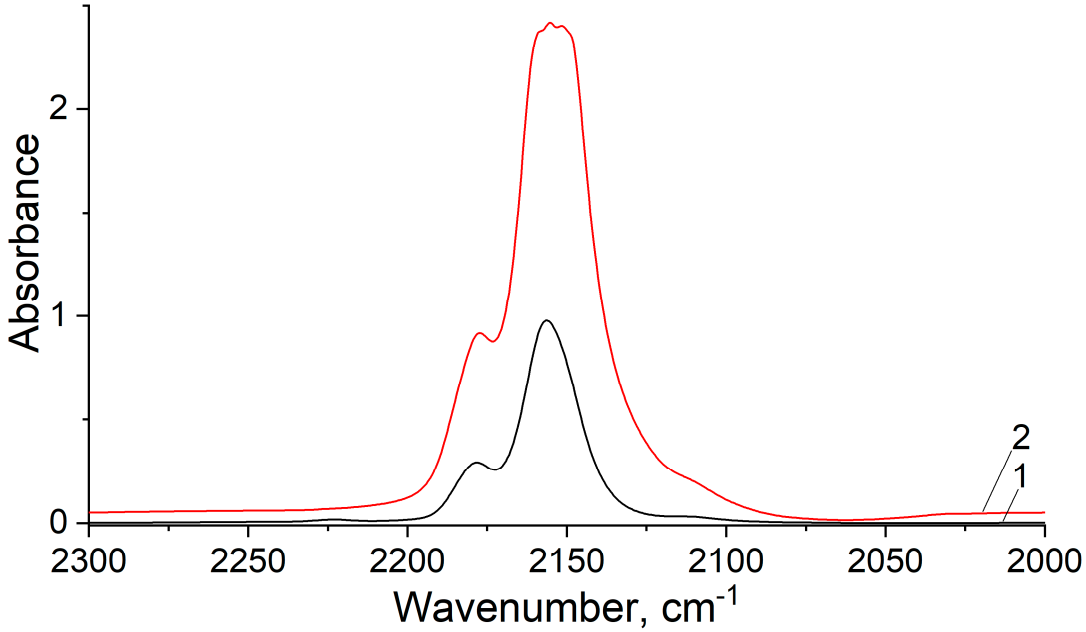

Figure S5 Difference FTIR spectra of CO adsorbed on MOR ion-exchanged (one) and impregnated (two) by $Cu(NO_3)_2$ solution

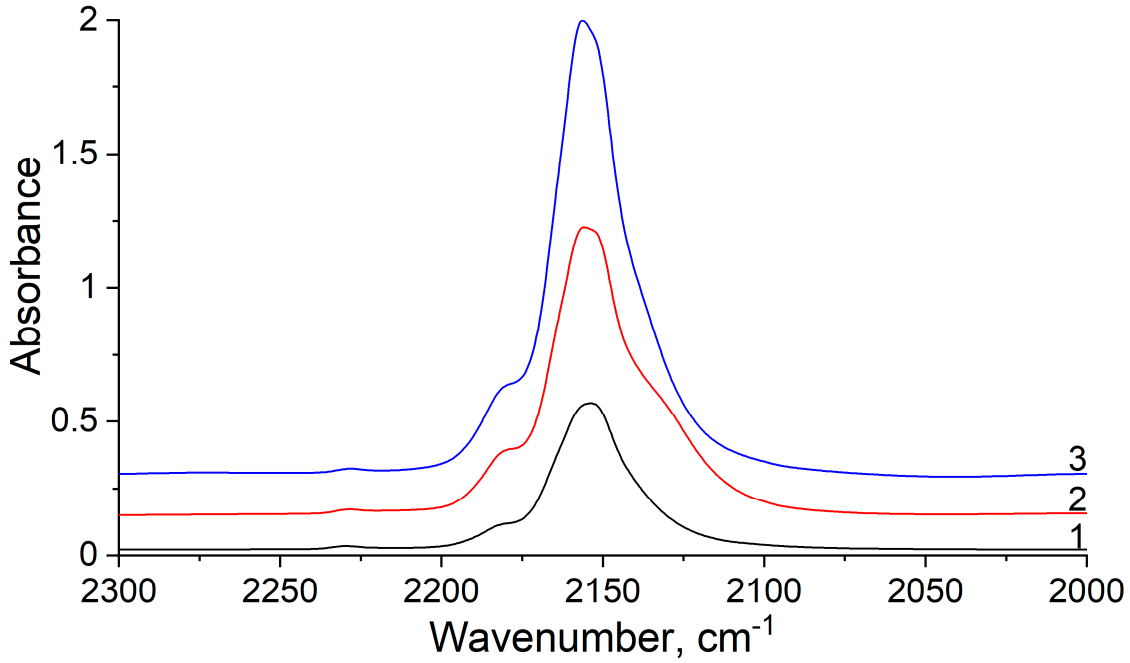

Figure S6 Difference FTIR spectra of CO adsorbed on BEA-12 impregnated with $CuSO_4$ (1), $Cu(NO_3)_2$ (2), $Cu(OAc)_2$ (3), spectra are offset for clarity.

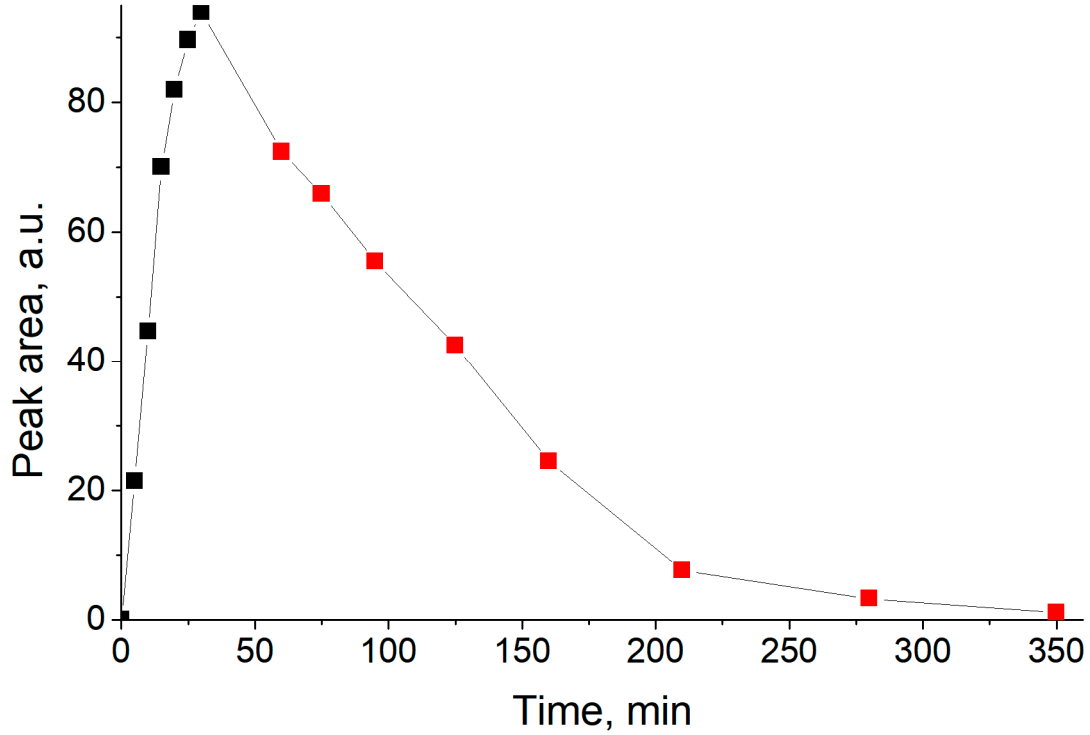

Figure S7 Time-dependent evolution of the IR peak area following CO adsorption on MOR-$Cu(NO_3)_2$ (black) and evolution of IR peak area during stepwise desorption at different temperatures of CO on MOR-$Cu(NO_3)_2$ (red).

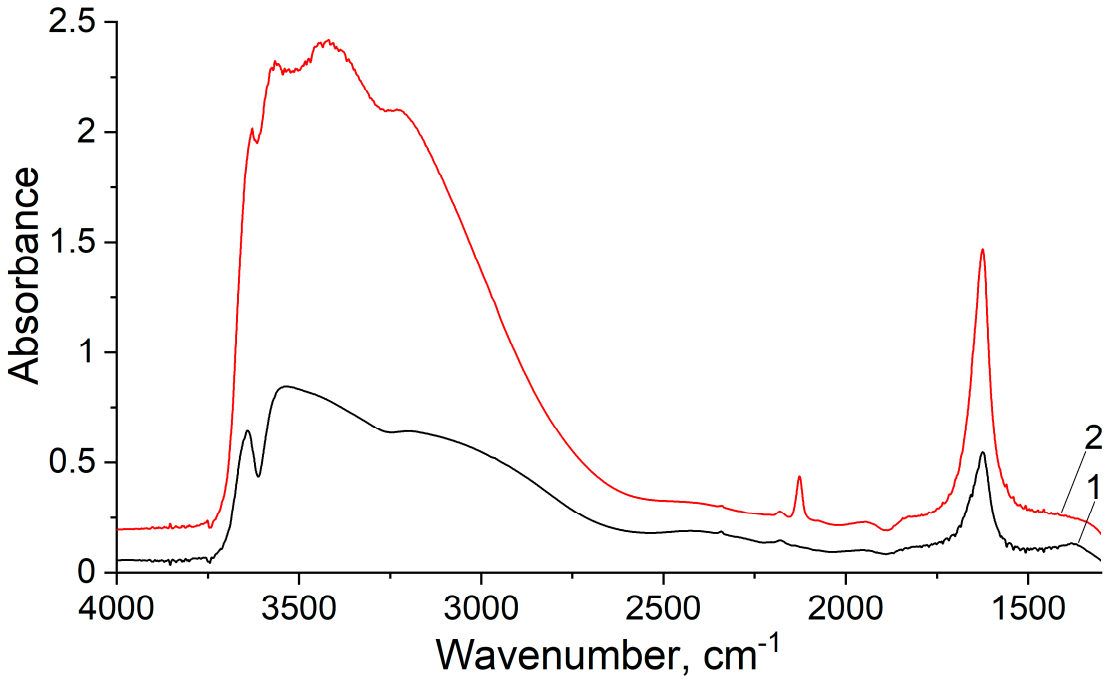

Figure S8 Difference FTIR spectra of $Cu(NO_3)_2$-impregnated MOR: exposed to air for 5 minutes (1), exposed to CO in the air for 2 minutes (2).

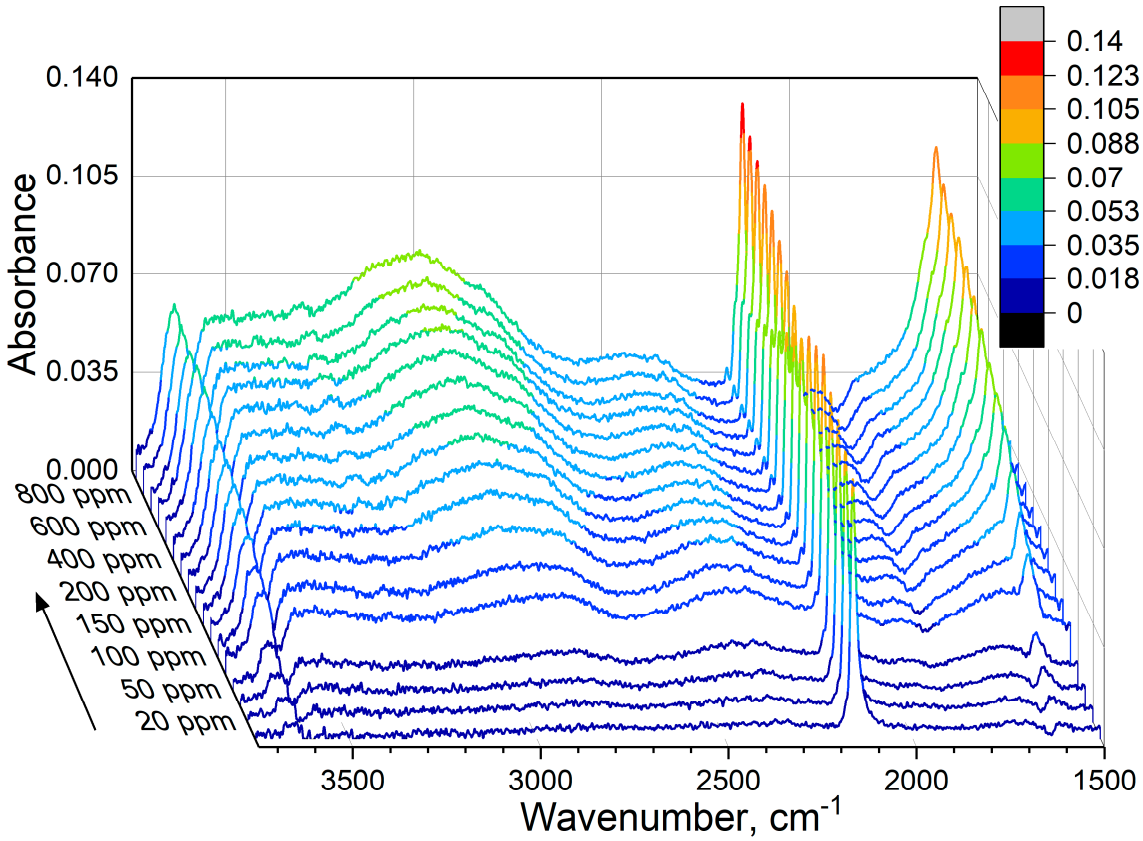

Figure S9 . Waterfall graph of difference FTIR spectra of CO adsorbed on CuMOR in Ar flow. For all waterfall sets of spectra, they are offset for clarity and the colour legend represents the absorbance scale.

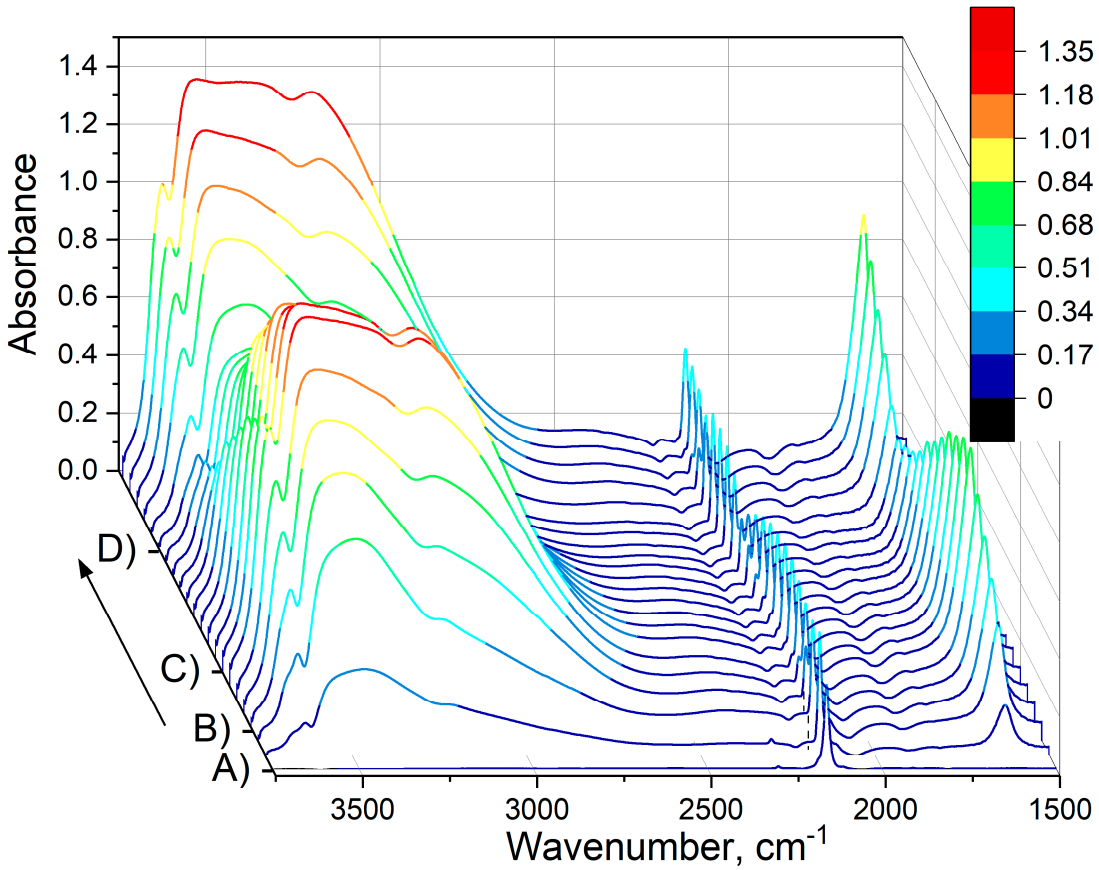

Figure S10 Waterfall graph of difference FTIR spectra of CO adsorbed on $Cu(NO_3)_2$-impregnated MOR, 50 ppm of CO adsorbed (step A) followed by stepwise H_2O adsorption (step B), evacuation (step C) and H_2O re-adsorption (step D).

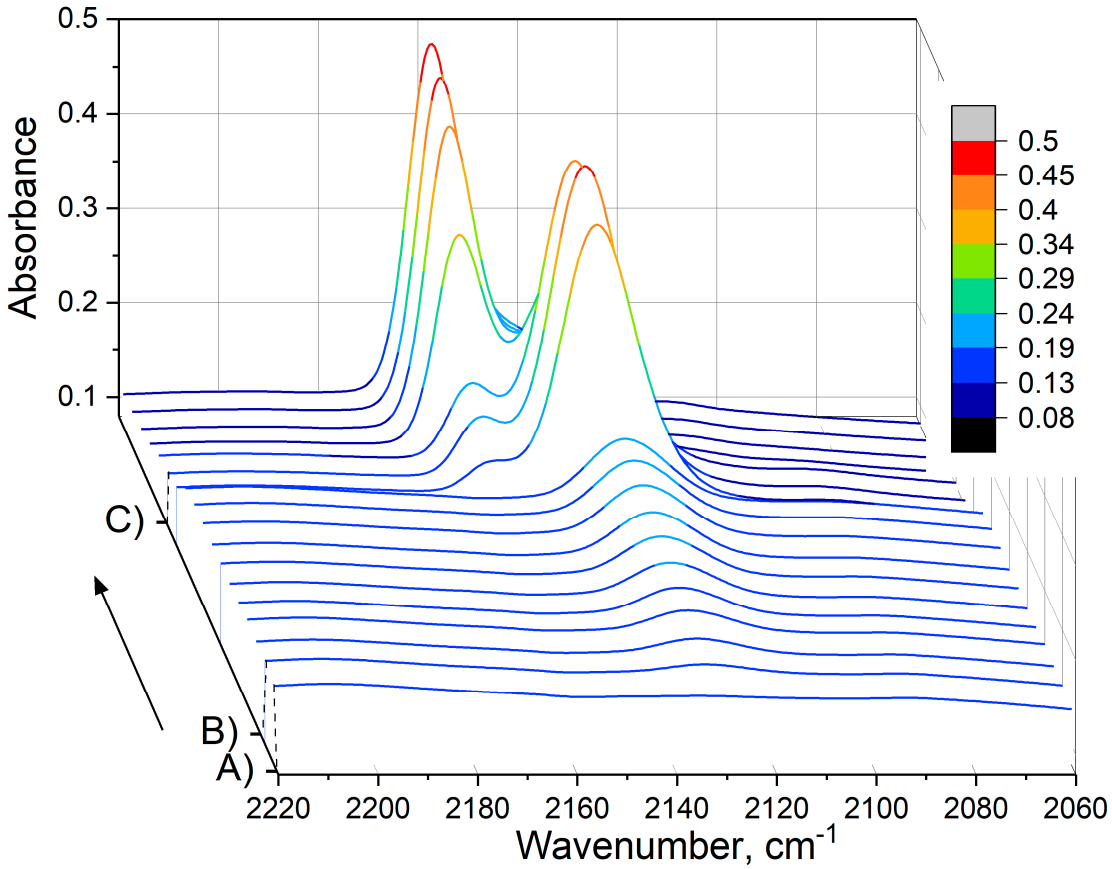

Figure S11 Waterfall graph of difference FTIR spectra of CO adsorbed on $Cu(NO_3)_2$-impregnated MOR after 1µL H_2O adsorption (step A), followed by CO introduction at different partial pressures (50-1000 ppm) (step B) and evacuation (step C).

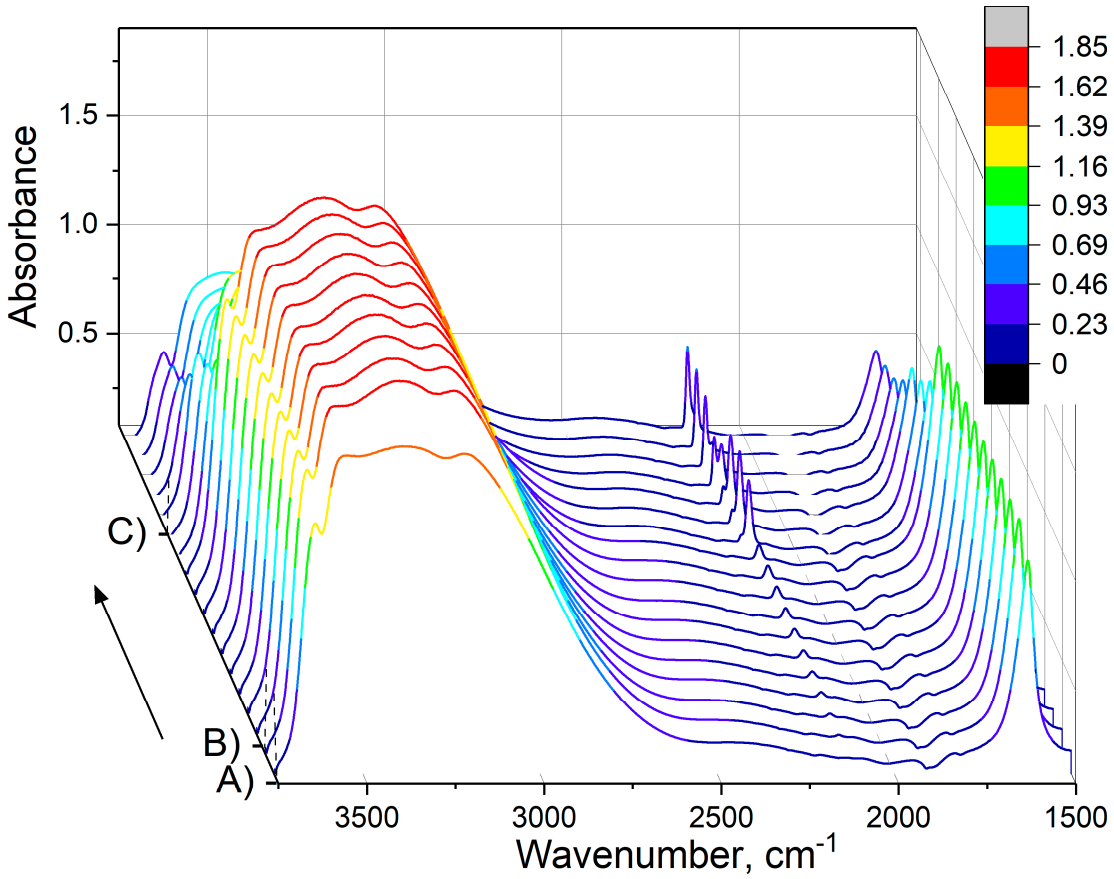

Figure S12 Waterfall graph of difference FTIR spectra of CO adsorbed on $Cu(NO_3)_2$-MOR after 1µL H_2O adsorption (step A), followed by CO introduction at different partial pressures (50-1000 ppm) (step B) and evacuation (step C).

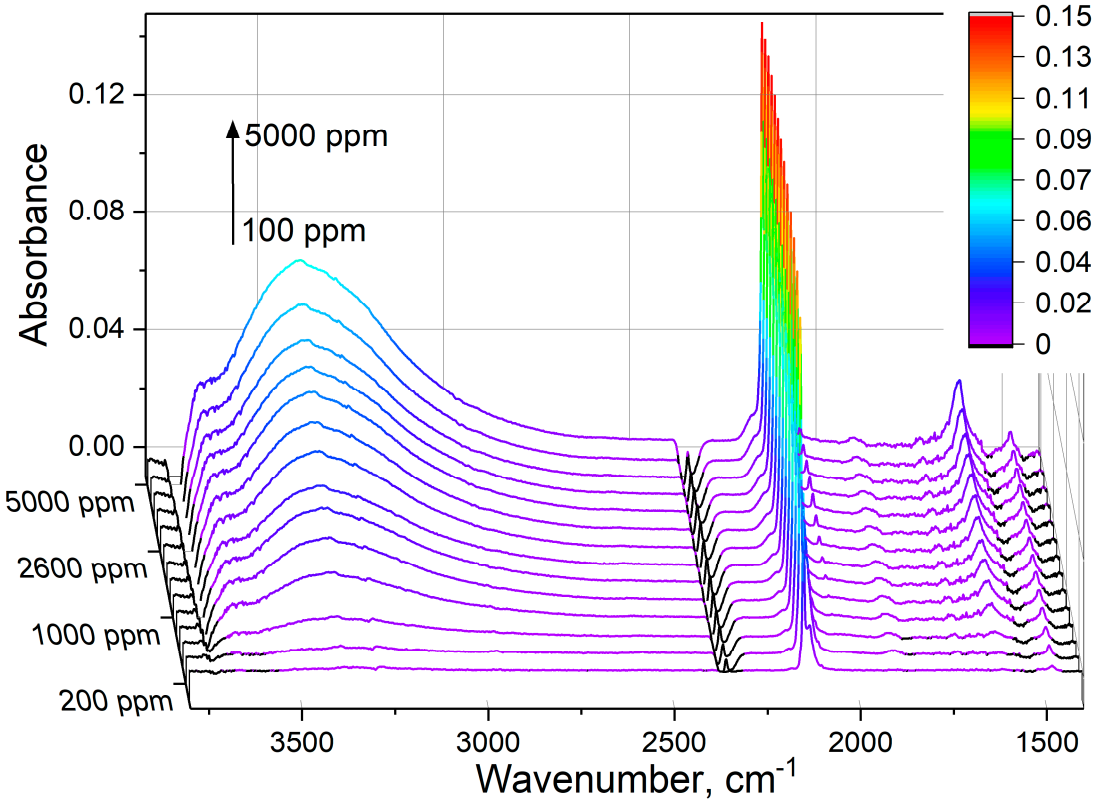

Figure S13 Difference FTIR spectra of CO adsorbed on CuSn-BEA, 100-5000 ppm (in Ar flow containing 100 ppm of water vapour).

In vacuo CO – H_2O coadsorption on CuSn-BEA

To evaluate the effect of water on CO adsorption on CuSn-BEA, an equivalent of 50 ppm of CO was introduced into the in situ vacuum cell (Figures S13-S15, step A), followed by step B, that is stepwise addition of 0.1 µL H_2O to the total of 0.5 µL. In contrast to $Cu(NO_3)_2$-MOR (Figures 7a and 7b), the intensity of the 2149 cm^{-1} peak is decreasing and the broad peak centred at 2132 cm^{-1} splits into two unresolved peaks at 2138 and 2133 cm^{-1}. The reversibility of water adsorption was tested by desorption over 45 minutes (step C), during which the intensity of the 2149 cm^{-1} peak has completely recovered. Subsequently, during the water re-adsorption step (step D), a total of 1.6 µL of H_2O (an equivalent of ~2400 ppm) was required to fully red-shift the 2149 cm^{-1} band to 2132 cm^{-1}.

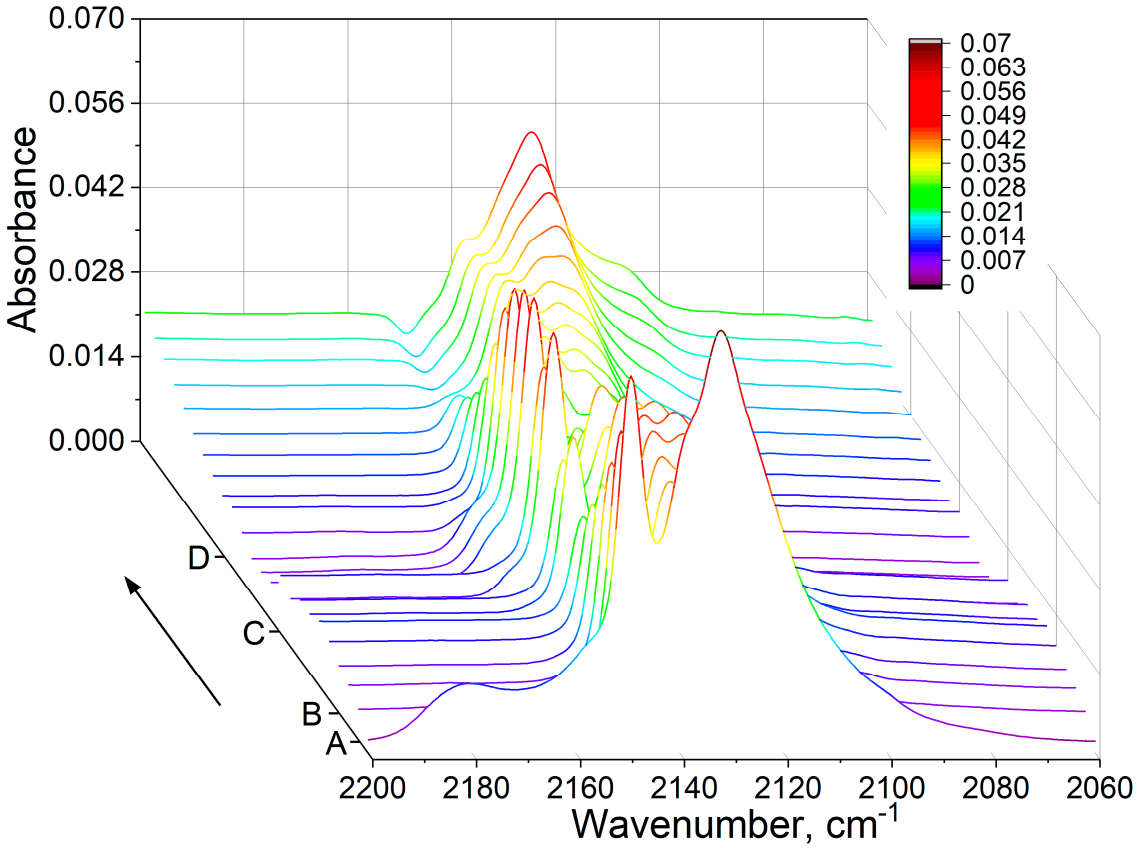

Figure S14 Waterfall graph of difference FTIR spectra of CO adsorbed on CuSn-BEA (step A), water interference experiment (step B) and desorption experiment (step C) and water readsorption (step D).

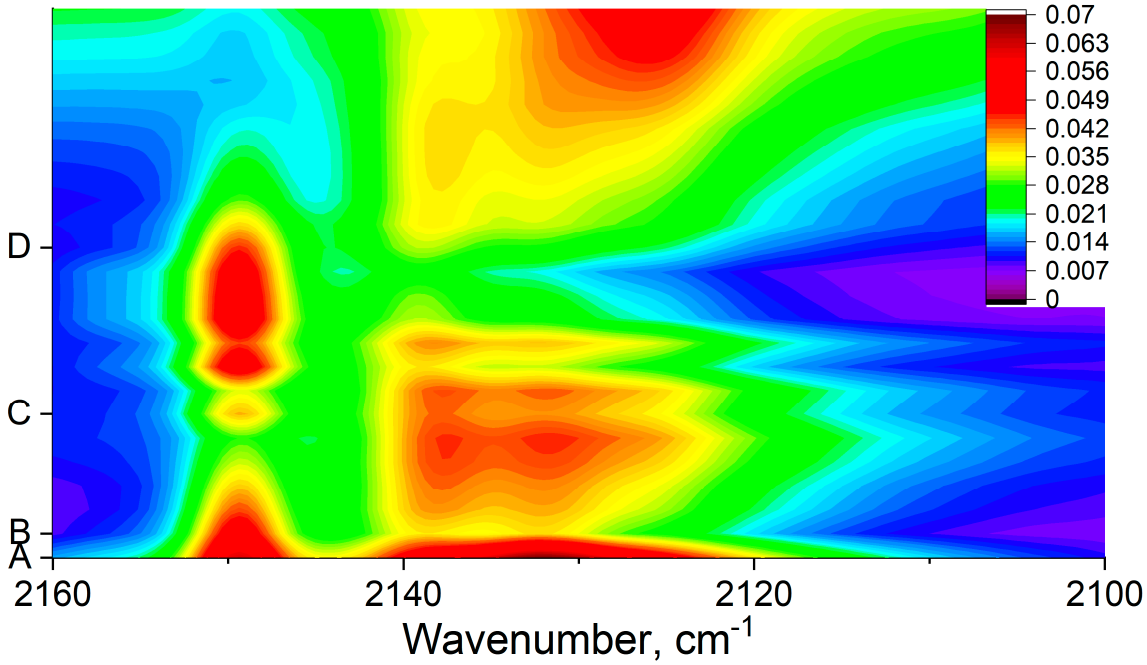

Figure S15 2D contour map of difference FTIR spectra of CO adsorbed on CuSn-BEA (step A), water interference experiment (step B) and desorption experiment (step C) and water re-adsorption (step D), colour legend represents the absorbance scale.

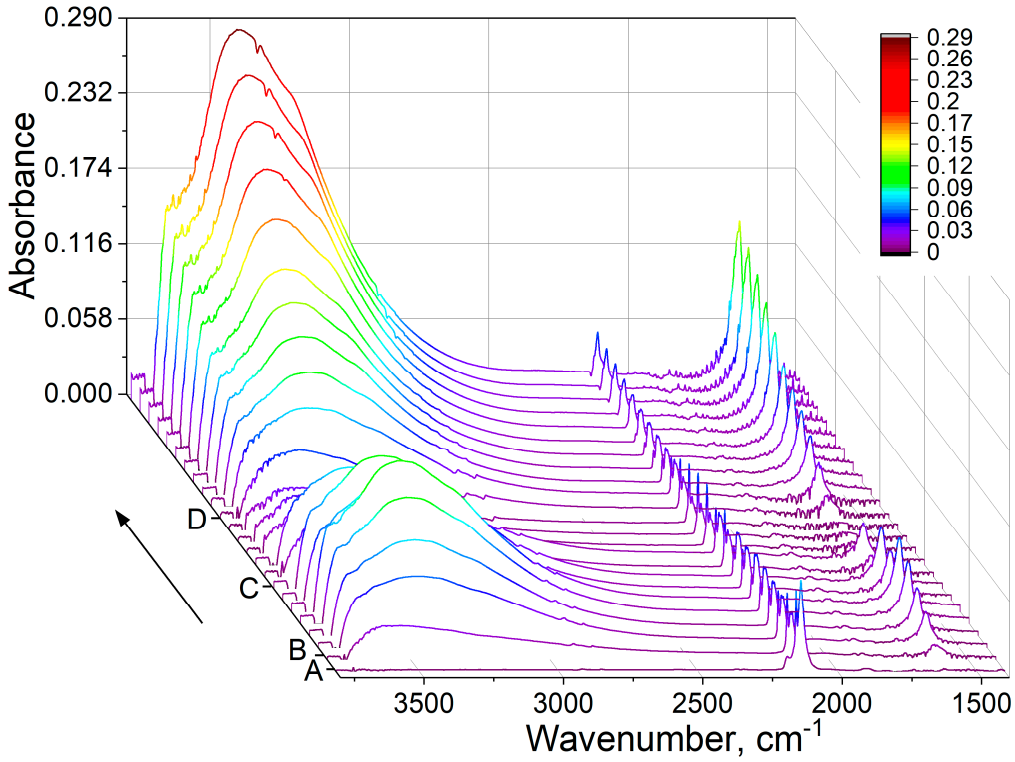

Figure S16. Waterfall graph of difference FTIR spectra of CO adsorbed on CuSn-BEA (step A), water interference experiment (step B) and desorption experiment (step C) and water readsorption (step D).

Finally, the CuSn-BEA sensor has been subjected to CO titration in the presence of H_2O (an equivalent of ~1500 ppm, Figure S17). It can be observed that the 2149 cm^{-1} peak is less intense than the broad peak centred at 2130 cm^{-1}. At lower CO concentrations, the unresolved peaks at 2138 and 2133 cm^{-1} are observed, which at higher CO concentrations are centred at 2129 cm^{-1} (see also Figure 10a). The broad peak is marginally red-shifted to 2129 cm^{-1}, but the water vapour is not interfering with the peak evolution, as it does with the MOR-$Cu(NO_3)_2$ (Figure S11).

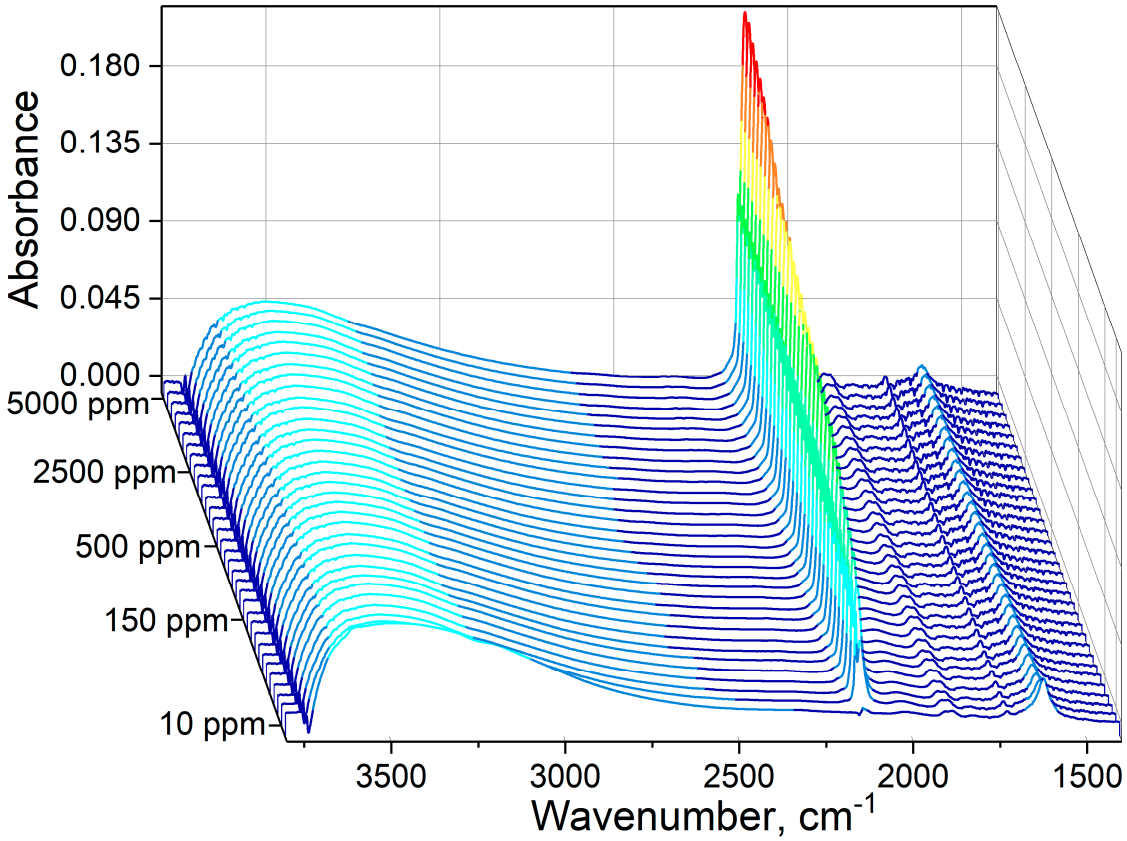

Figure S17. Waterfall graph of difference FTIR spectra of CuSn-BEA in vacuo after saturation with ~1500 ppm of H_2O followed by CO adsorption, 10 to 5000 ppm.

Supplementary information: Supplementary Characterisation File

N_2 adsorption – desorption isotherms

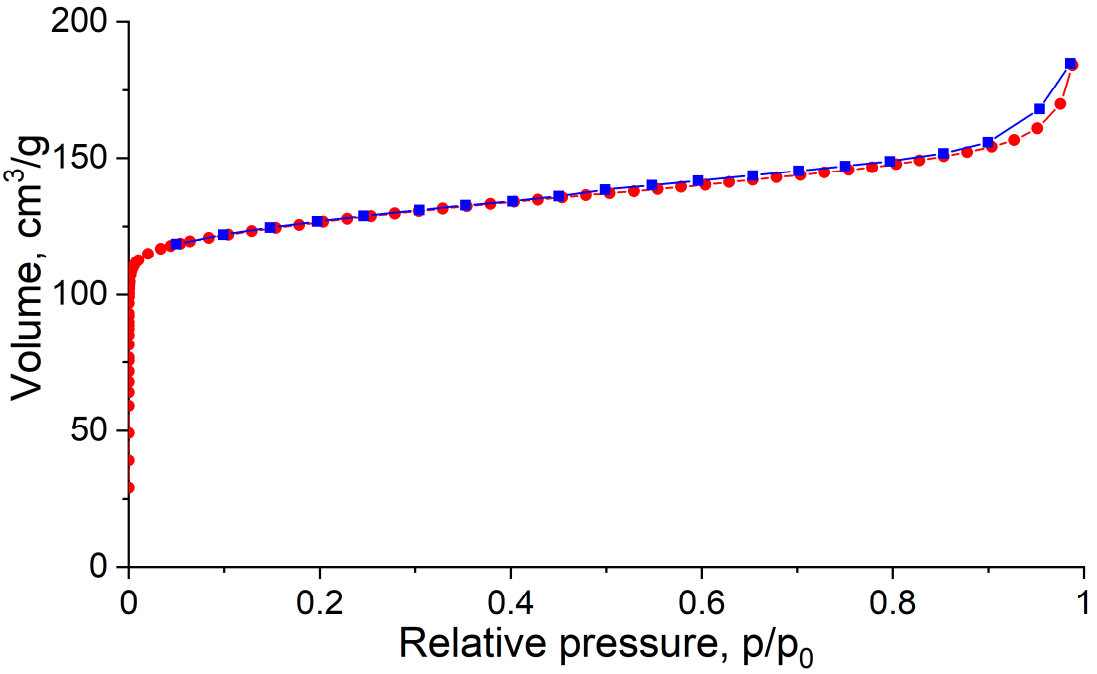

Figure S18 N_2 adsorption-desorption isotherm of NH_4-MOR.

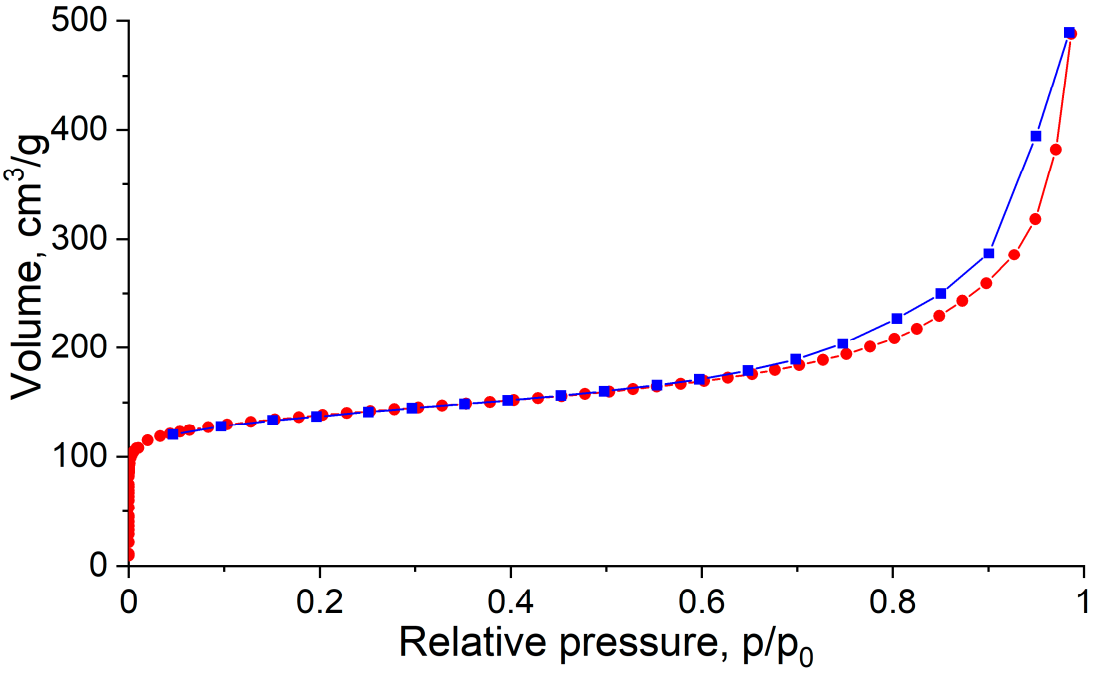

Figure S19 N_2 adsorption-desorption isotherm of BEA-12.

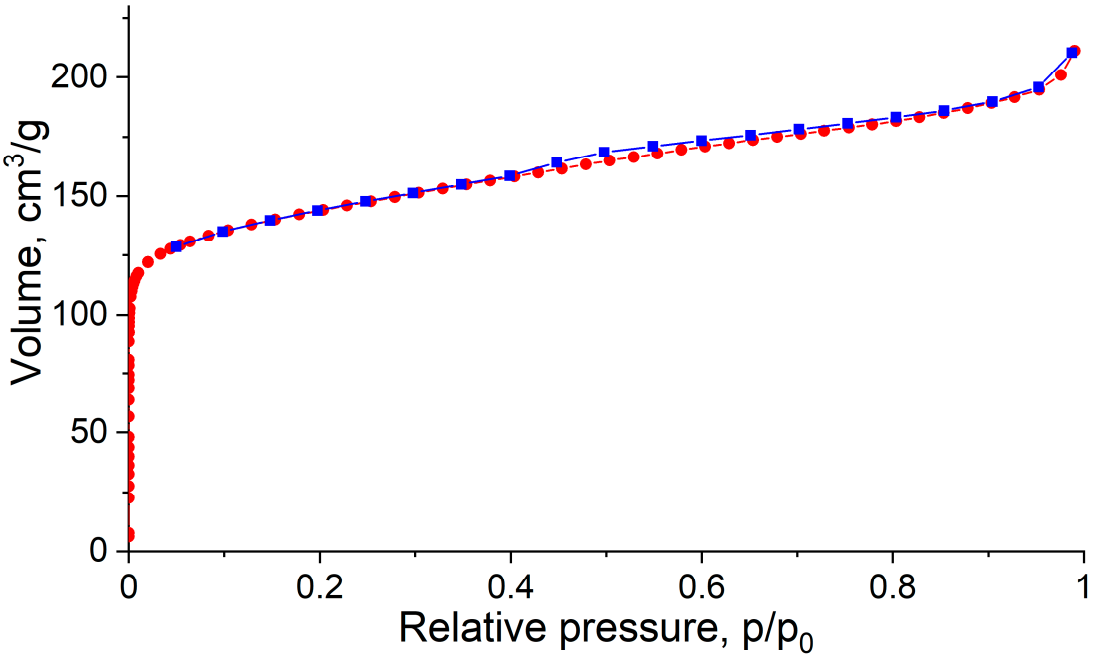

Figure S20 N_2 adsorption-desorption isotherm of BEA-19.

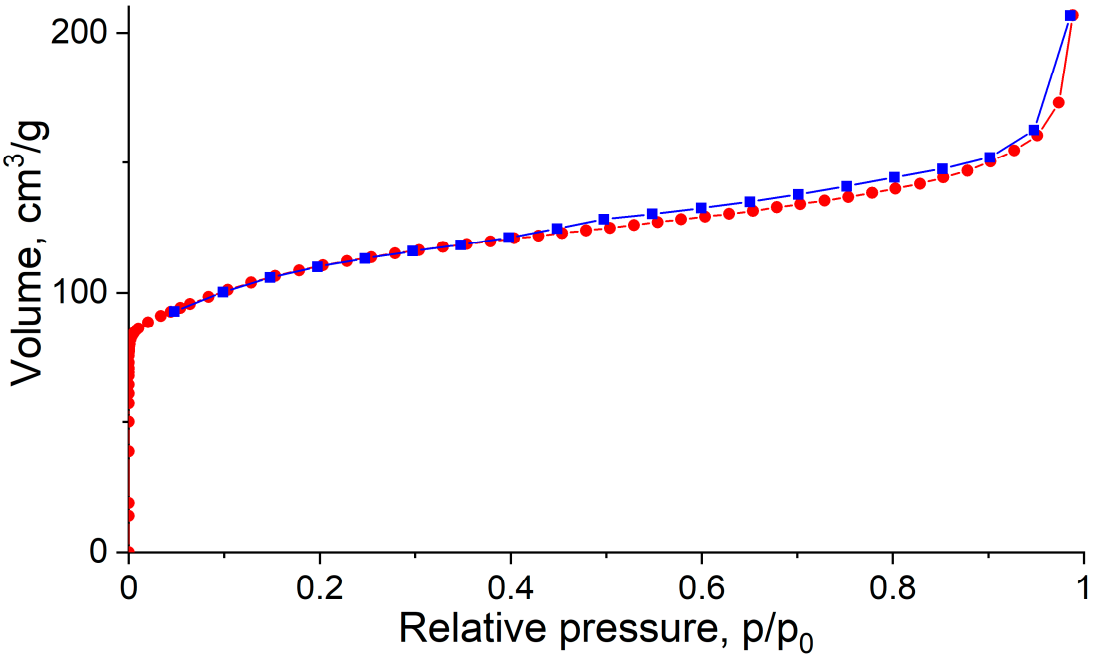

Figure S21 N_2 adsorption-desorption isotherm of ZSM-5.

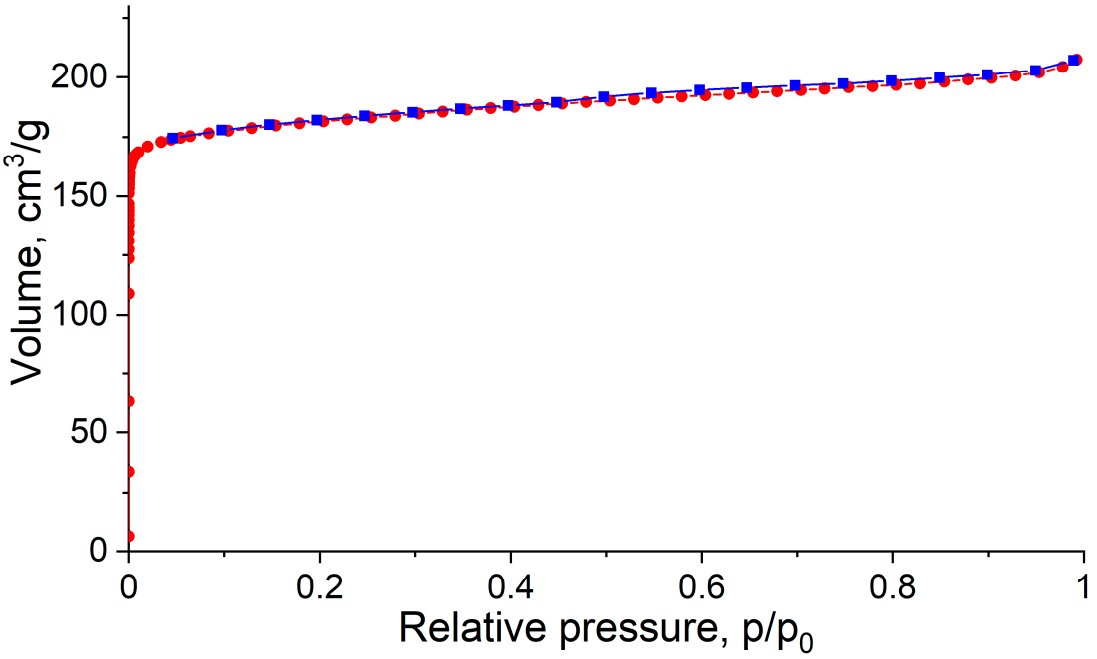

Figure S22 N_2 adsorption-desorption isotherm of NaX.

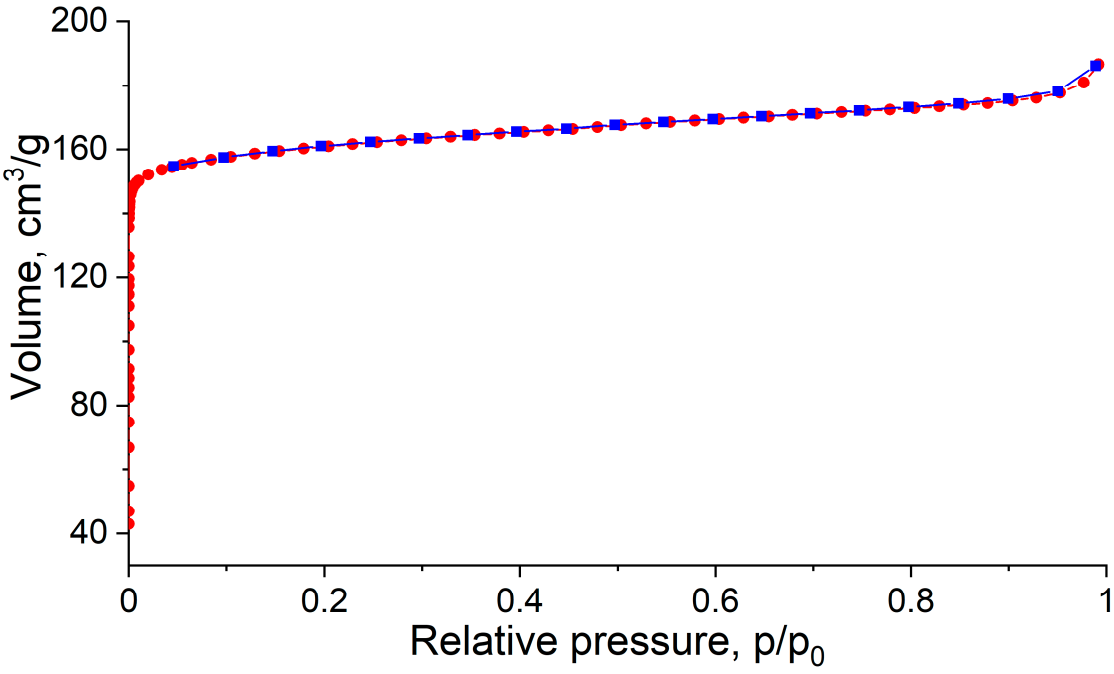

Figure S23 N_2 adsorption-desorption isotherm of NaY.

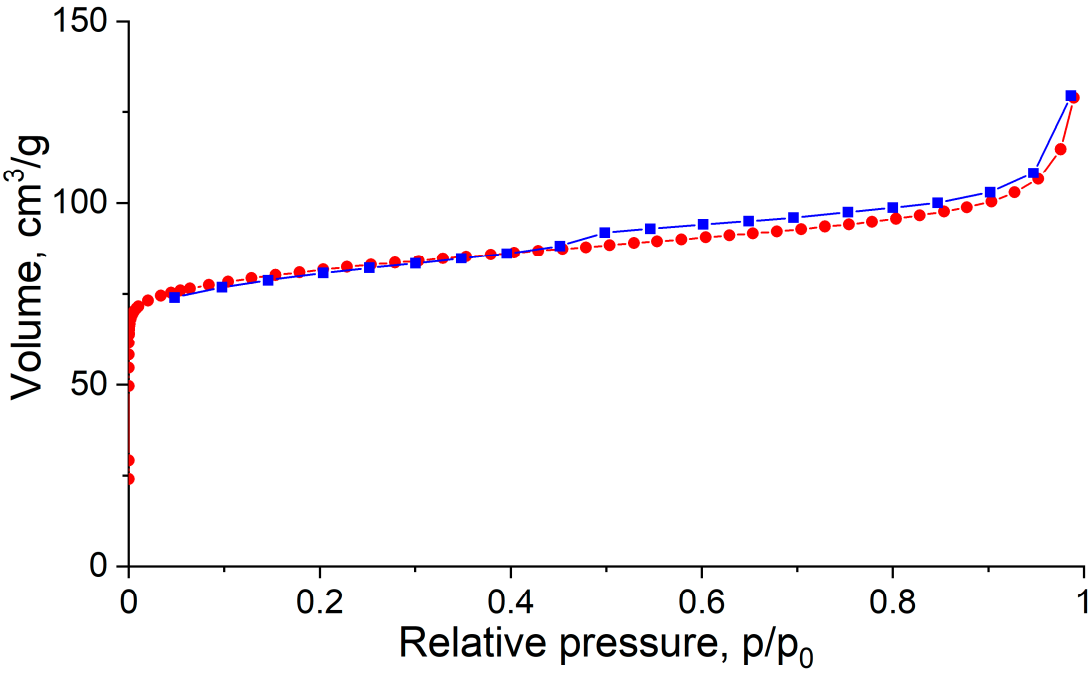

Figure S24 N_2 adsorption-desorption isotherm of FER.

Powder X-ray diffraction patterns (XRD)

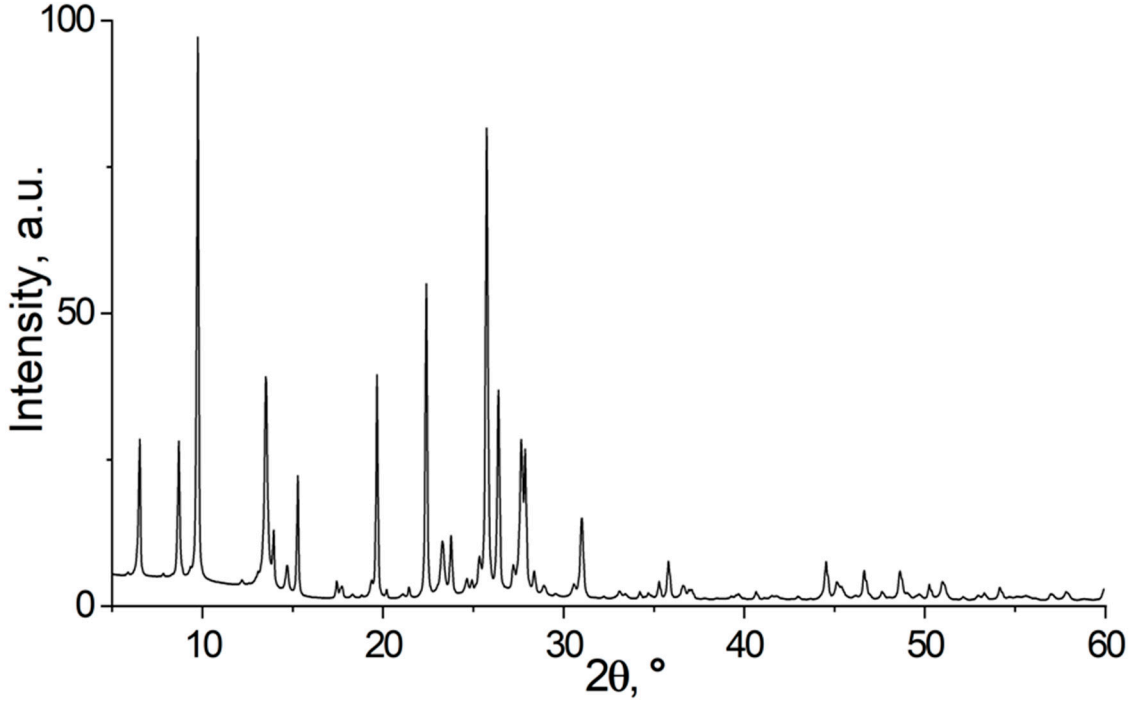

Figure S25 XRD pattern of MOR

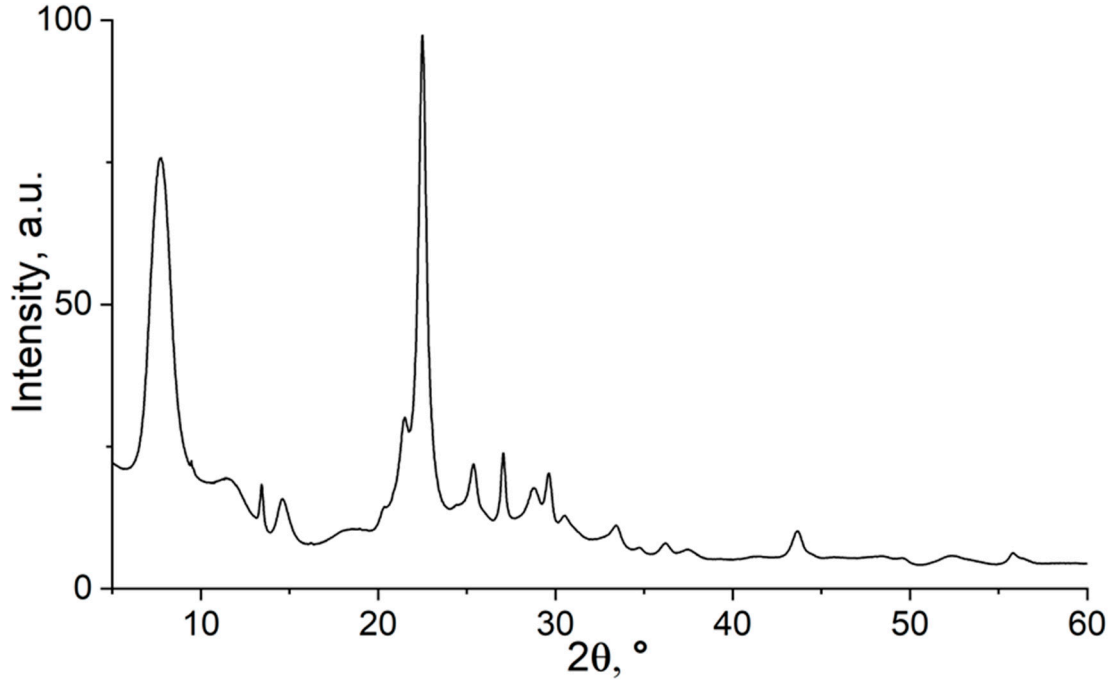

Figure S26 XRD pattern of BEA 12

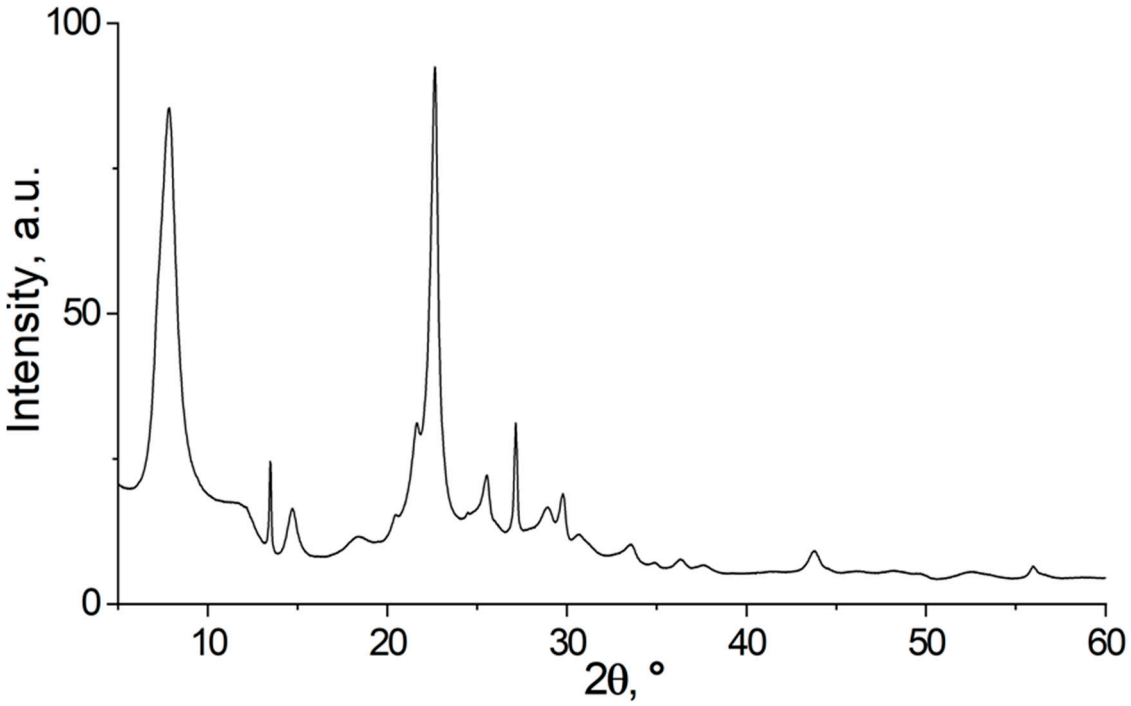

Figure S27 1 XRD pattern of BEA 19

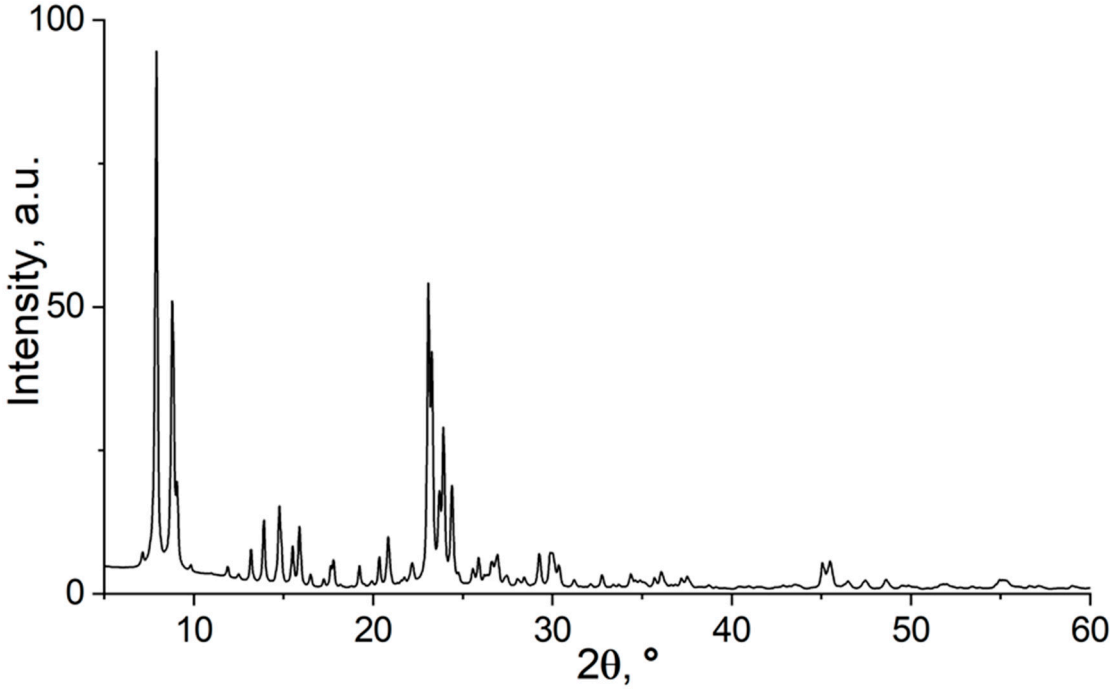

Figure S28 XRD pattern of ZSM-5

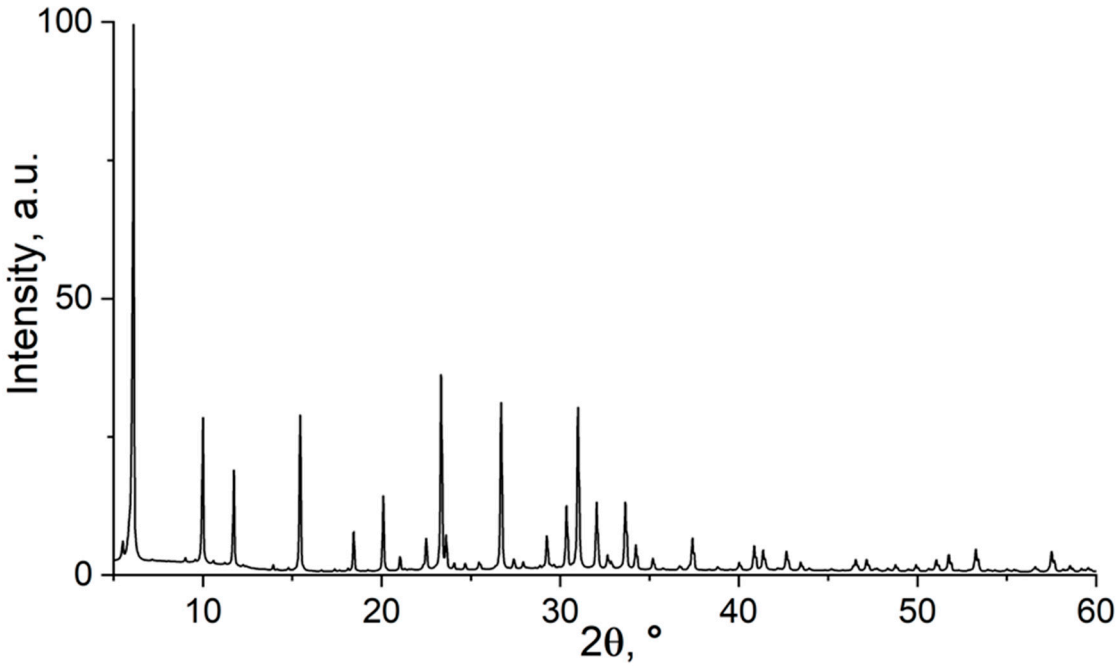

Figure S29 XRD pattern of NaX

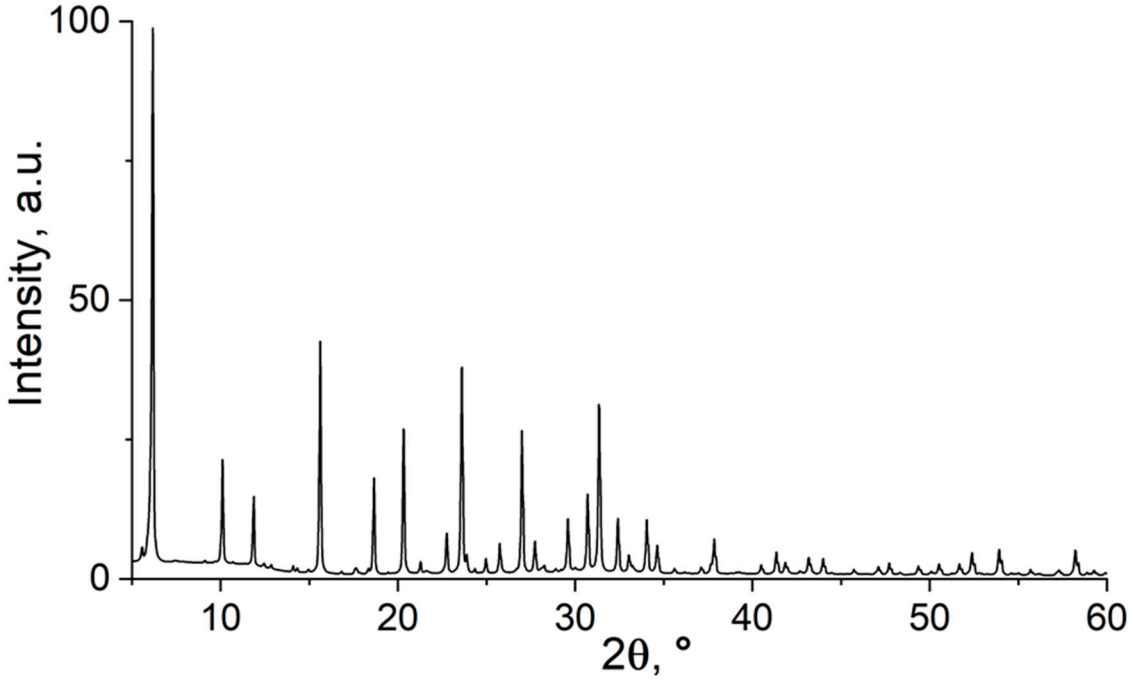

Figure S30 XRD pattern of NaY

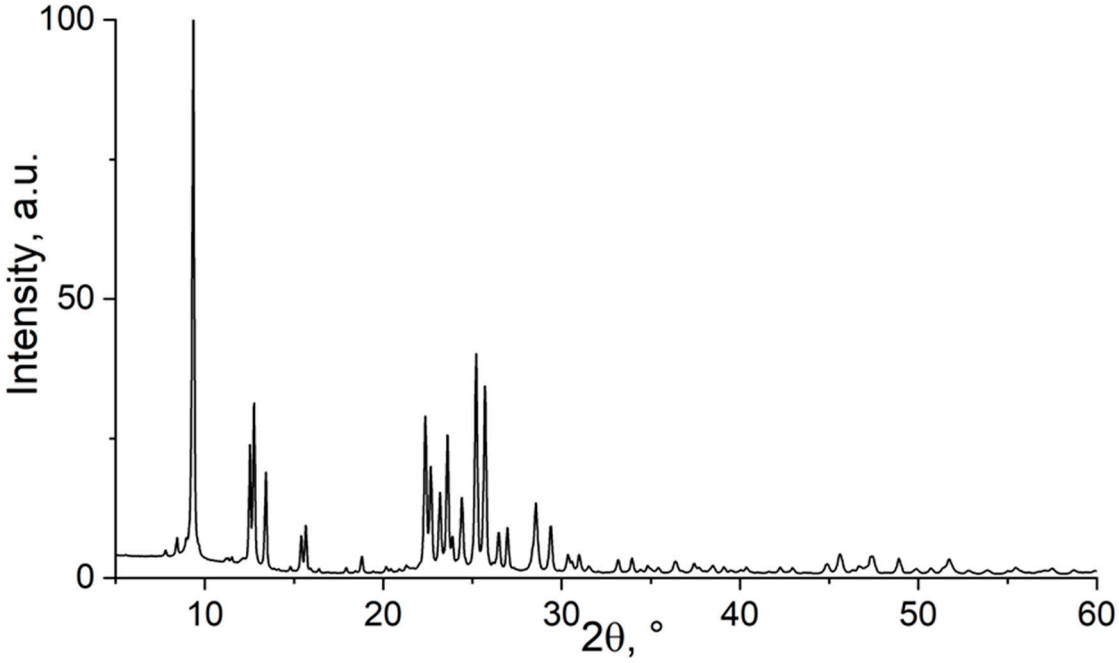

Figure S31 XRD pattern of FER

Thermogravimetric analysis (TGA) curves

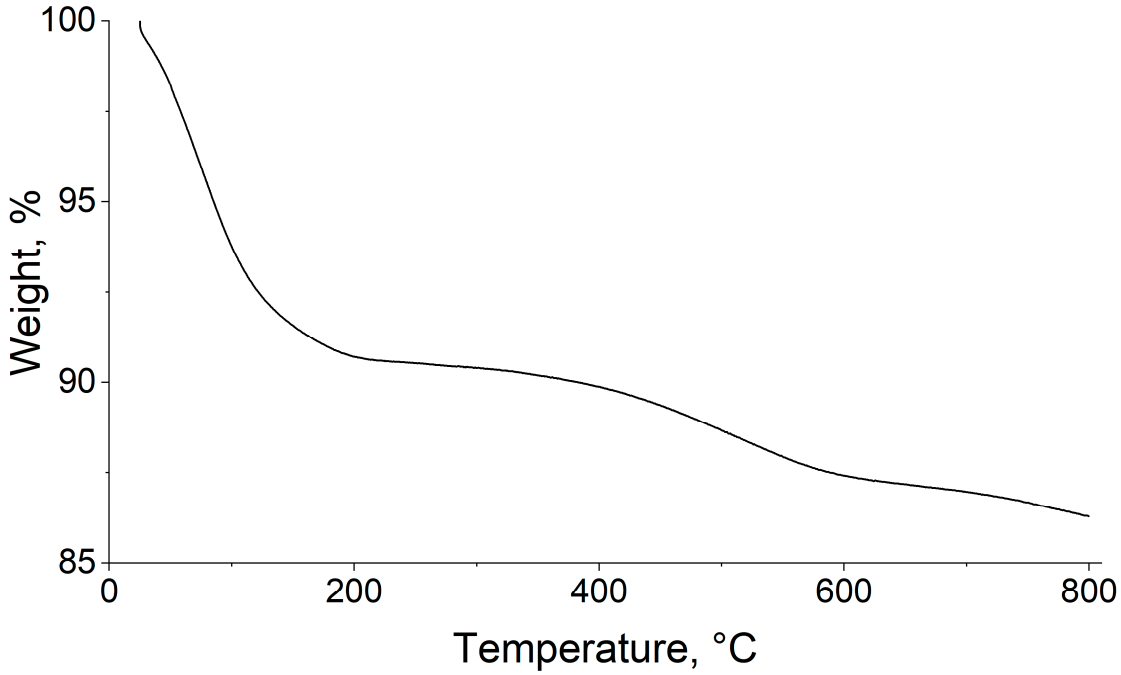

Figure S32 TGA curve of MOR.

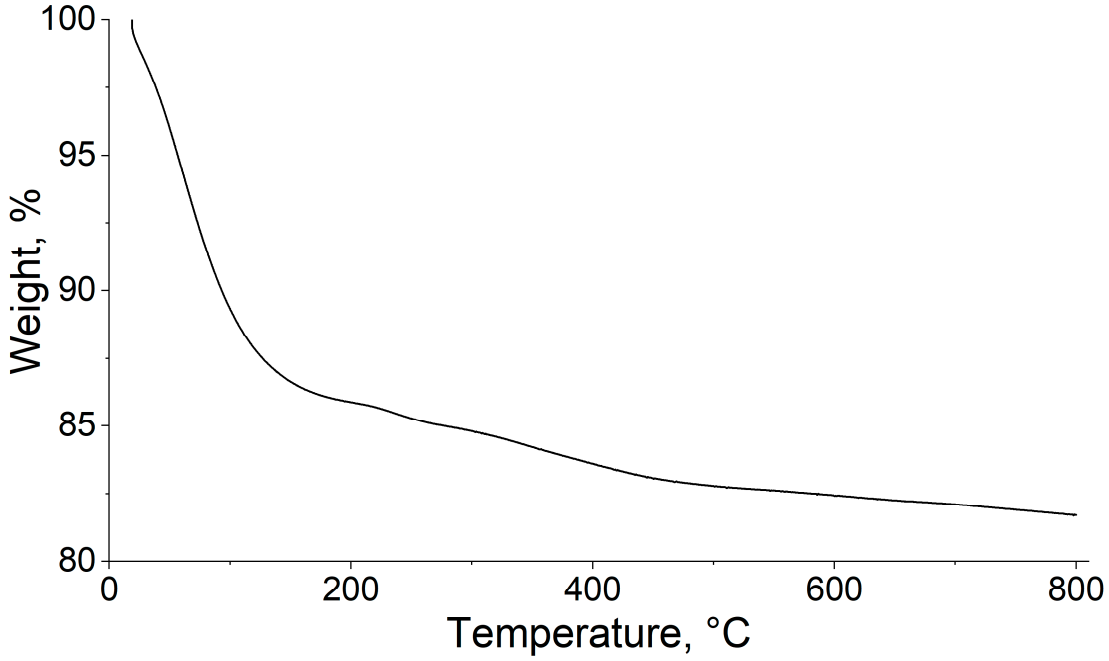

Figure S33 TGA curve of BEA-12.

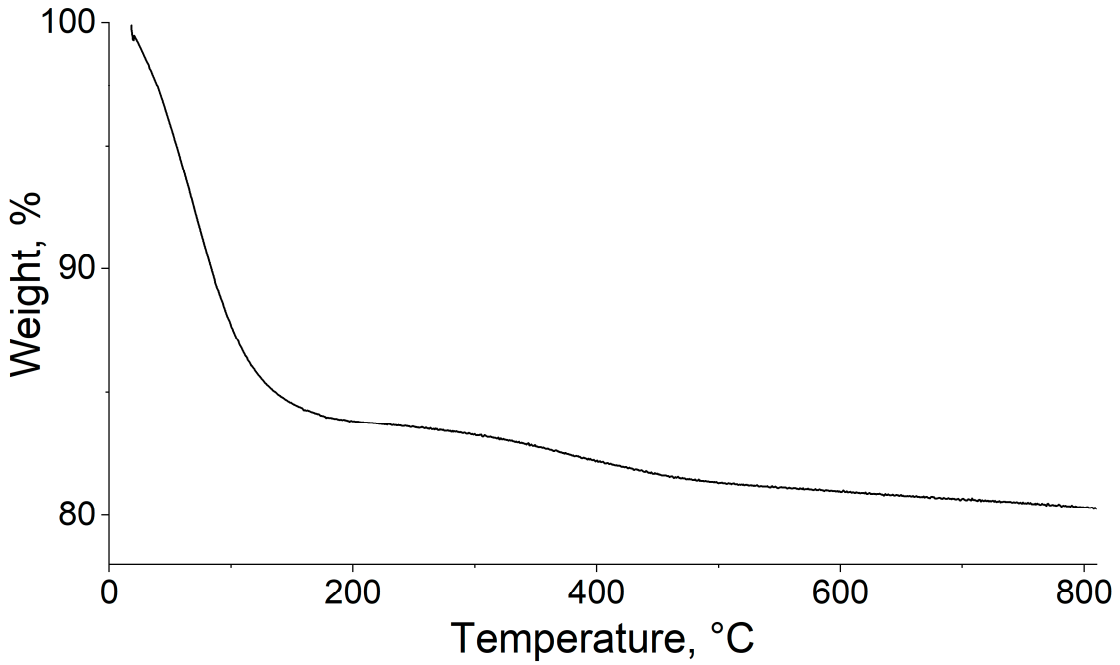

Figure S34 TGA curve of BEA-19.

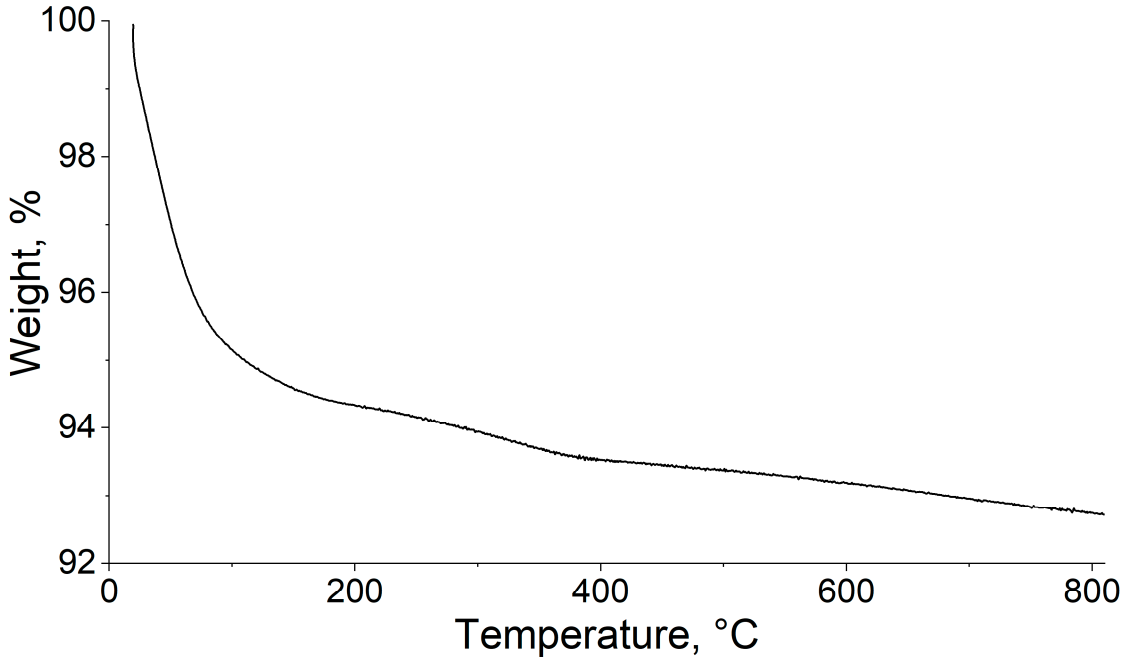

Figure S35 TGA curve of ZSM-5.

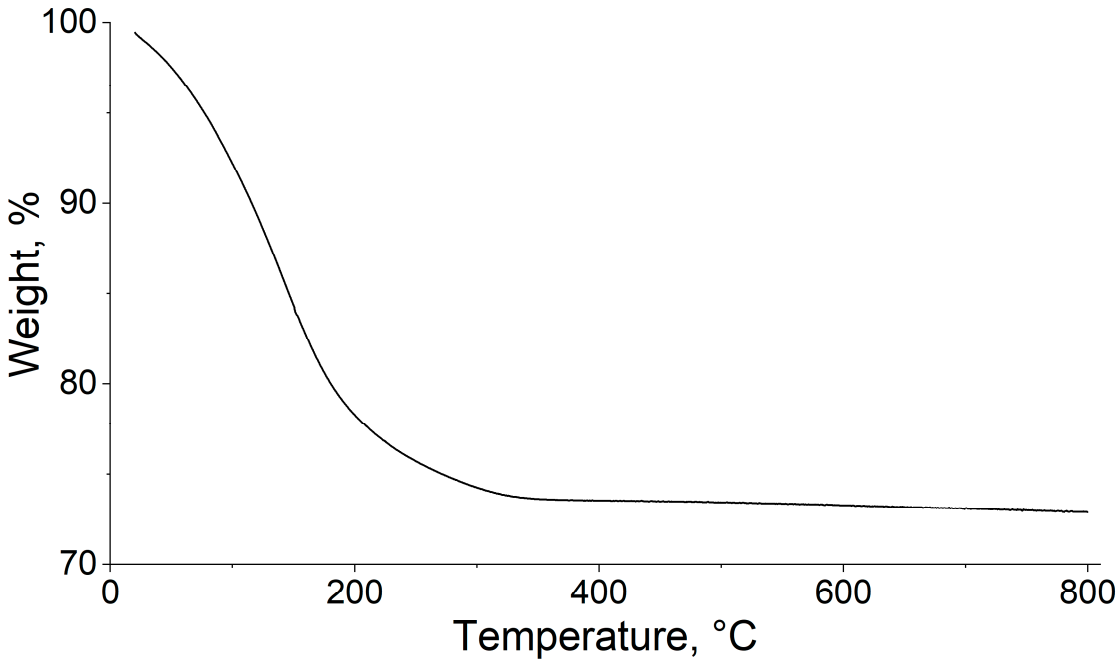

Figure S36 TGA curve of NaX.

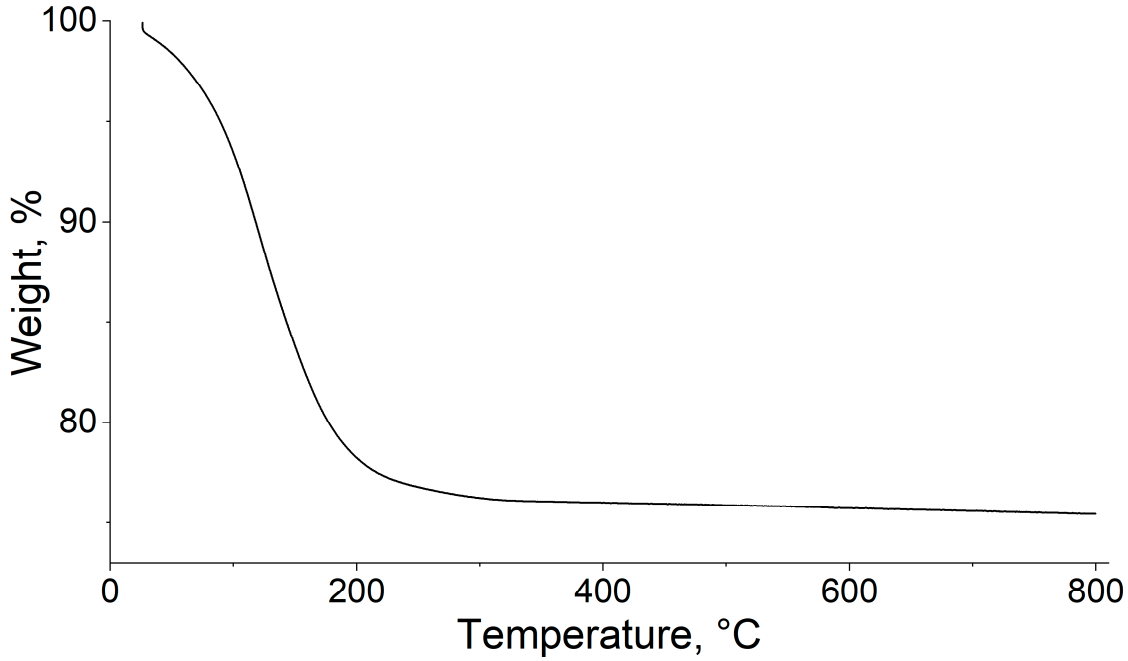

Figure S37 TGA curve of NaY.

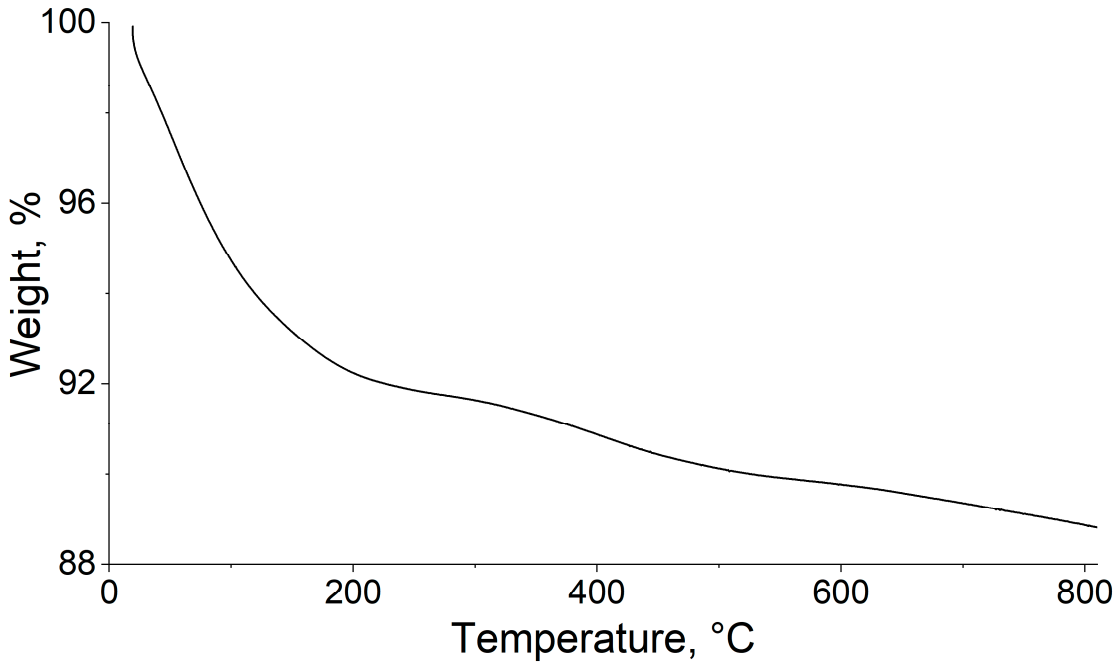

Figure S38 TGA curve of FER.

Table S2 TGA weight loSC data of reference samples at 200 °C and 400 °C.

Zeolite	Weight loSC at 200 °C, %	Weight loSC at 400 °C, %
MOR	9.3	10.12
BEA 12	14.13	16.4
BEA 19	16.2	17.79
ZSM-5	5.67	6.48
NaX	21.74	26.45
NaY	21.77	24.01
FER	7.76	9.14

FTIR spectra

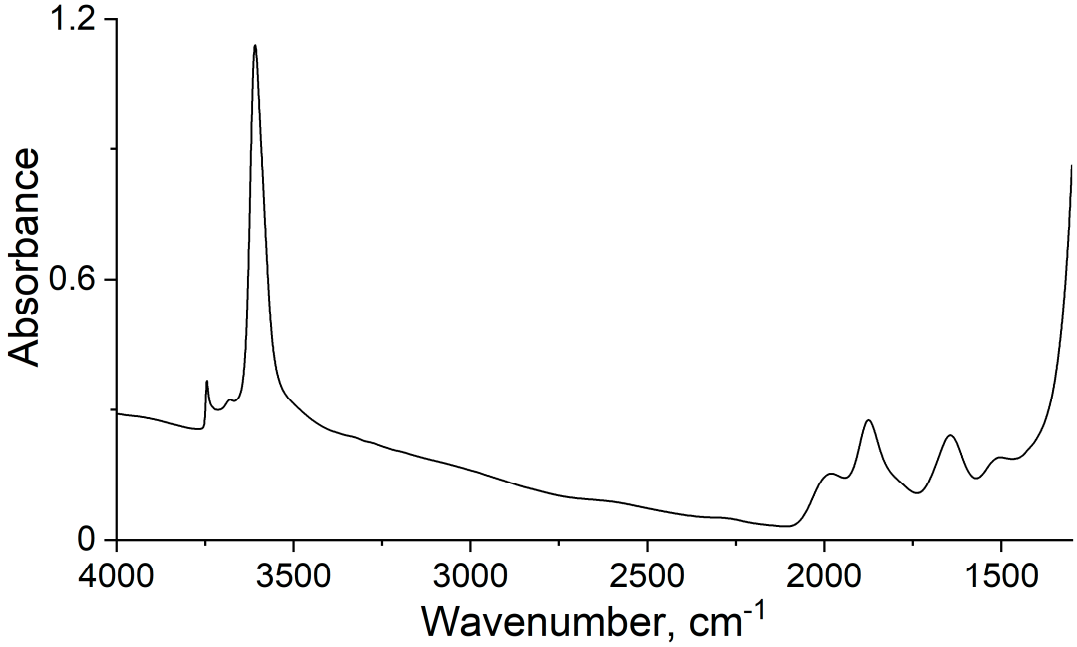

Figure S39 FTIR spectrum of MOR

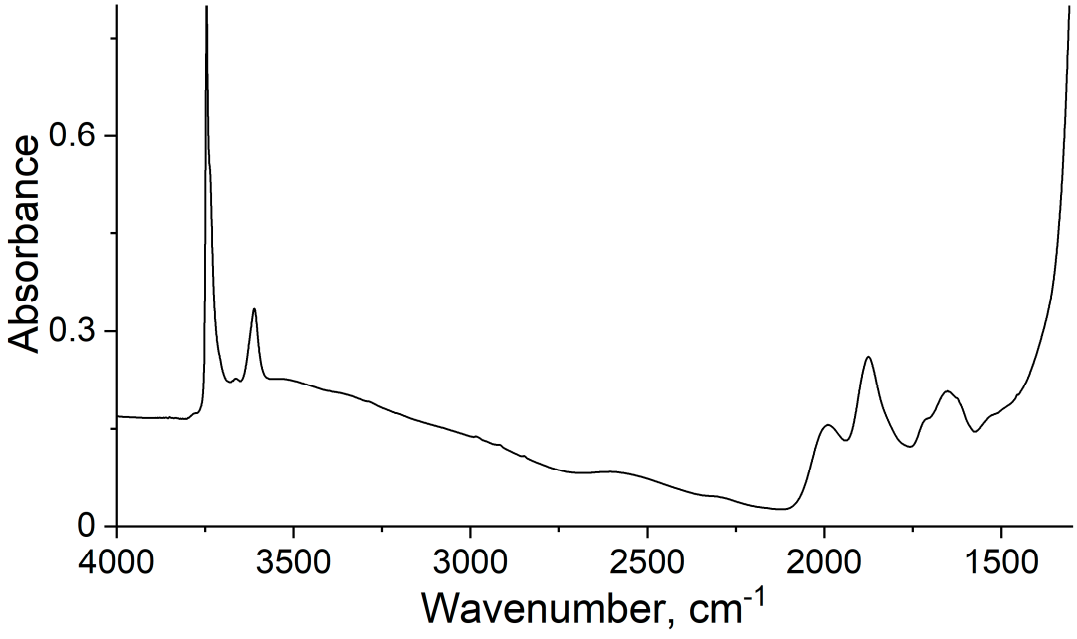

Figure S40 FTIR spectrum of BEA-12

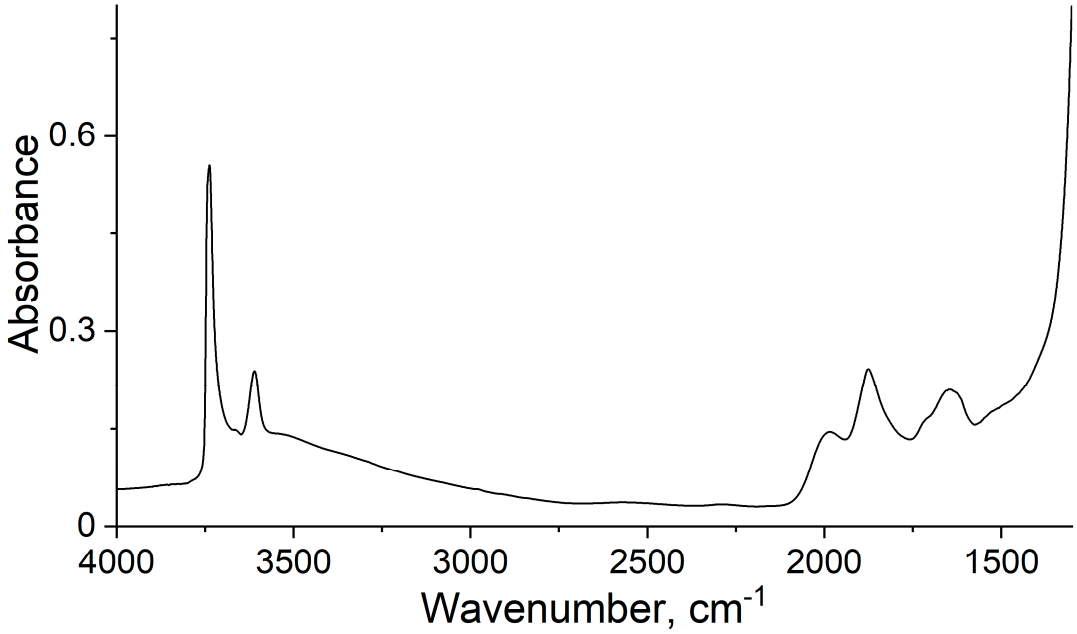

Figure S41 FTIR spectrum of BEA-19

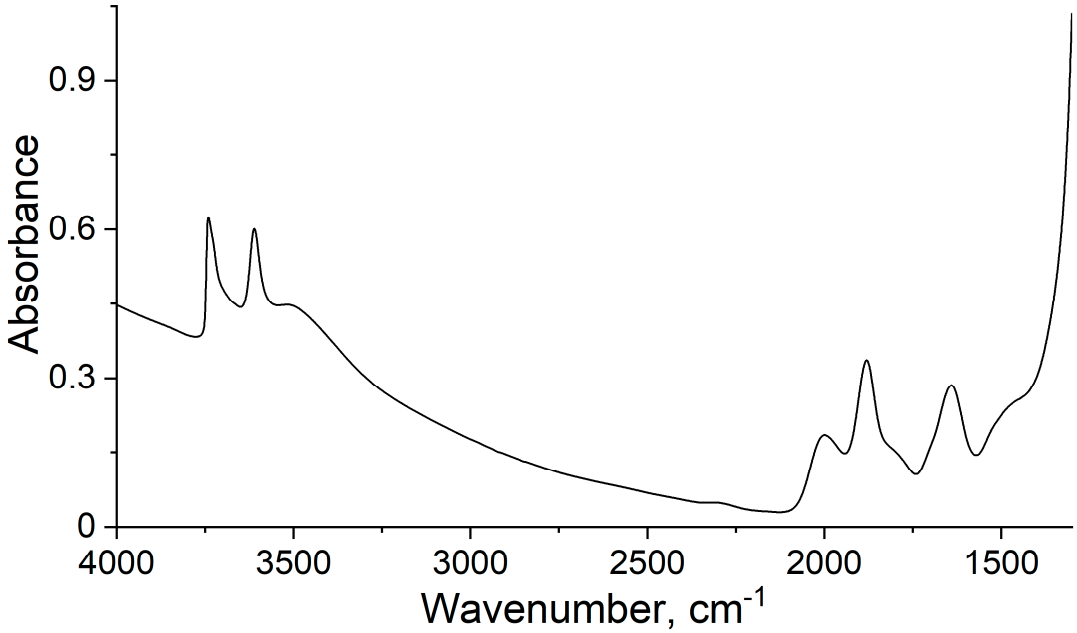

Figure S42 FTIR spectrum of ZSM-5

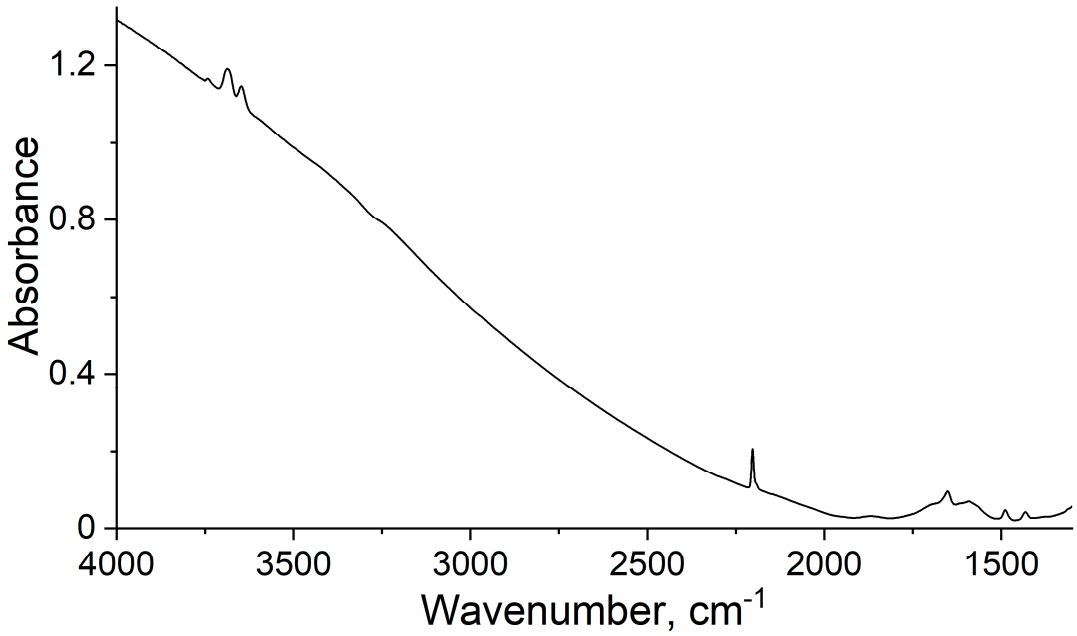

Figure S43 FTIR spectrum of NaX

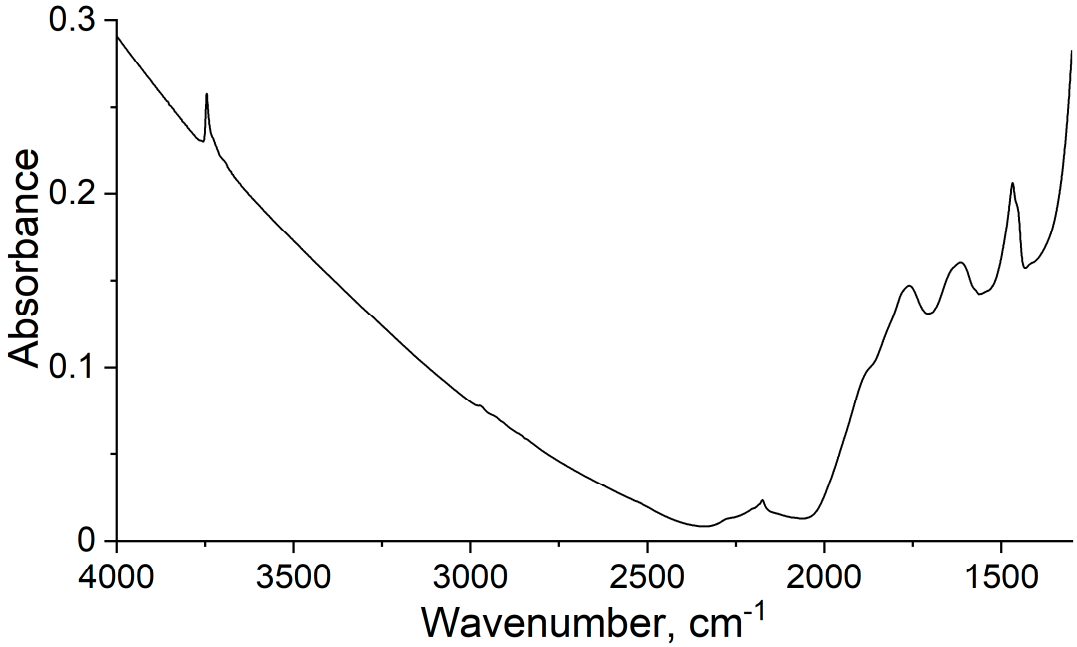

Figure S44 FTIR spectrum of NaY

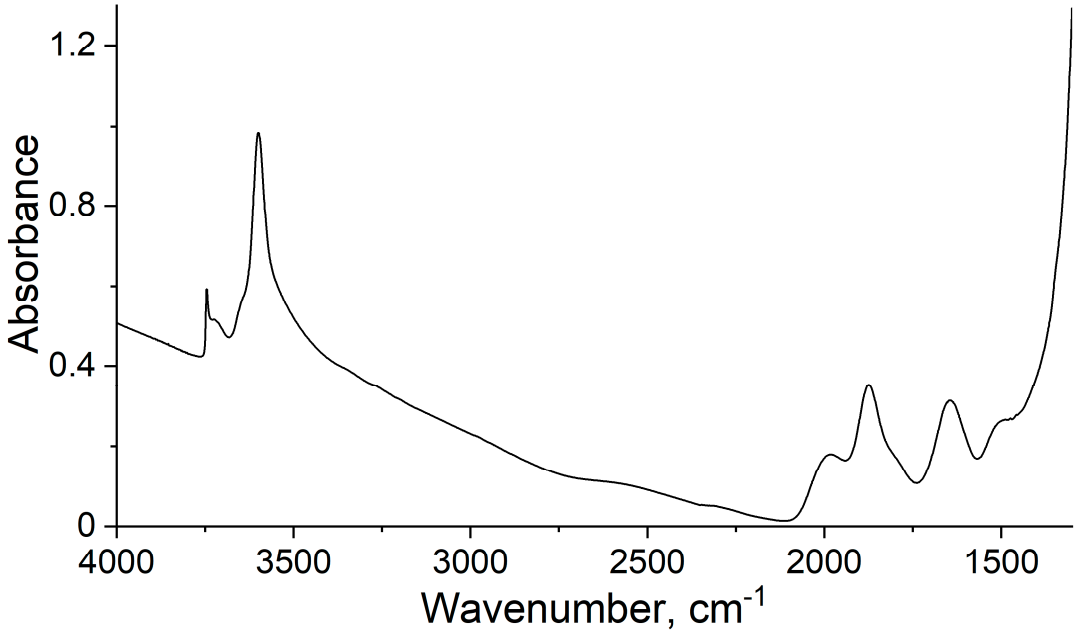

Figure S45 FTIR spectrum of FER

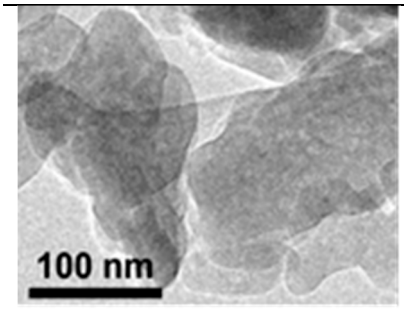	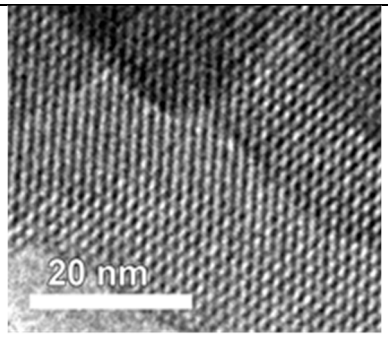	ZSM-5
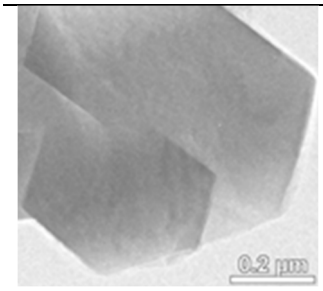	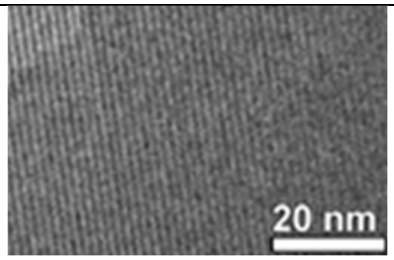	Na-Y
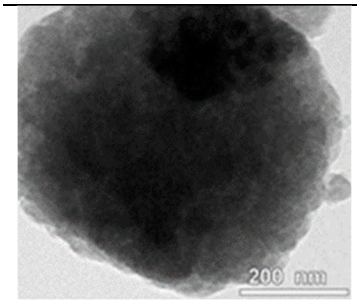	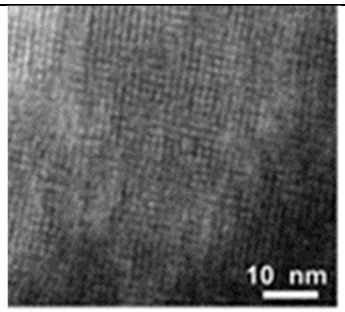	BEA-19
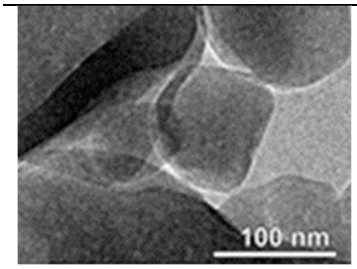	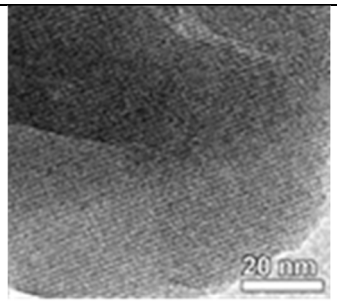	MOR

Figure S46 Electron microscopy data for selected zeolites.